KRT17 Promotes T-lymphocyte Infiltration Through the YTHDF2–CXCL10 Axis in Colorectal Cancer

Wenfeng Liang[1,2,3], Huashan Liu[1,2,3], Ziwei Zeng[1,2,3], Zhenxing Liang[1,2,3], Hao Xie[1,2,3], Wenxin Li[1,2,3], Li Xiong[1,2,3], Zhihang Liu[1,2,3,4], Mian Chen[1,2,3], Haiqing Jie[1,2,3], Xiaobin Zheng[1,2,3], Liang Huang[1,2,3], and Liang Kang[1,2,3]

ABSTRACT

Poor infiltration of T lymphocytes has been regarded as a crucial mechanism of tumor immune escape. Here, we demonstrate a protective role of KRT17 in colorectal cancer, where KRT17 reversed the tumor immunosuppressive microenvironment by increasing T-lymphocyte infiltration. High-throughput RNA sequencing suggested that KRT17 was significantly upregulated in deficient mismatch repair (dMMR) tumors compared with proficient mismatch repair (pMMR) tumors. In a colorectal cancer cohort of 446 cases, KRT17 expression positively correlated with better clinical outcomes. *Krt17* overexpression decreased xenograft tumor growth in immune-competent mice. T-cell depletion in a murine model showed that the presence of T lymphocytes was necessary for *Krt17*-mediated disruption of tumorigenesis. Mass spectrometry and coimmunoprecipitation assays suggested KRT17 caused YTHDF2 degradation through the ubiquitin-proteasome system. Through high-throughput RNA immunoprecipitation sequencing, we found that CXCL10 was the target gene of the N6-methyladenosine (m^6A) "reader" YTHDF2. KRT17 synergized with anti–PD-1 for better tumor control in an immunotherapy-resistant murine model. In a cohort of patients with colorectal cancer receiving pembrolizumab, high KRT17 expression was found within the tumors of responders. Collectively, we elucidated a critical role of KRT17 in colorectal cancer to prevent immune escape. These findings present new insights into potential therapeutic strategies and effective markers of immunotherapy reactivity against pMMR tumors.

Introduction

The immune system safeguards the host from most pathogens and aberrant cells through multifactorial mechanisms, including innate and adaptive effector approaches. A malfunctioning immune system can cause a variety of illnesses, including autoimmune conditions, tumorigenesis, and pathogenic infections. Extensive internal and extrinsic factors, such as defective immunological molecules (1) and the application of immunosuppressants (2), can result in restricted antitumor immune responses and tumor progression. Emerging clinical evidence has demonstrated that immune checkpoint inhibitors (ICI) have durable antitumor activity in multiple cancer types (3, 4). Understanding the mechanisms by which tumors compromise immunity will be crucial for disease prevention and therapeutic interventions.

Immune escape refers to a process by which tumor cells evade immunologic detection and/or eradication through multiple pathways, including genetic or epigenetic alterations, cellular cross-talk, and recruitment of suppressive cells to the tumor microenvironment (TME; ref. 5). Reduced T-lymphocyte infiltration into tumors is one of the critical mechanisms behind immune escape (6). Rapidly accumulating data have begun to elucidate that tumors inhibit T-lymphocyte infiltration through multiple pathways, including immunoediting of tumor neoantigens (7), modified chemokine expression profiles (8), hijacking of the T-cell checkpoint pathways (9), and abnormal vasculature (10). Approximately 85% of patients with colorectal cancer have almost no cytotoxic T-lymphocyte (CTL) infiltration, and these patients usually have poor survival outcomes and high recurrence risk (11, 12). However, the mechanisms governing T-lymphocyte infiltration in colorectal cancer remain largely unknown, and elucidating the potential regulatory mechanisms behind CTL infiltration is essential for developing effective strategies for tumor immunotherapy.

In this study, we identified a role and molecular mechanism of KRT17 in T-lymphocyte infiltration in colorectal cancer. To explore key factors that regulated CTL infiltration, RNA sequencing (RNA-seq) was performed to compare transcriptomic differences between deficient mismatch repair (dMMR) and proficient mismatch repair (pMMR) tumor tissues. We identified that KRT17 was highly expressed in dMMR tumors. In subcutaneous MC38 and CT26 models, *Krt17* overexpression increased T-lymphocyte infiltration to reverse immune escape. Mechanistically, KRT17 promoted ubiquitin-mediated degradation of YTHDF2, which decreased the decay of N6-methyladenosine (m^6A)-modified CXCL10 transcripts. Importantly, high KRT17 expression was found within the tumors of responders in a cohort of patients with colorectal cancer who had received pembrolizumab. In summary, these findings indicate that KRT17 is

[1]Department of General Surgery (Colorectal Surgery), The Sixth Affiliated Hospital, Sun Yat-sen University, Guangzhou, China. [2]Guangdong Provincial Key Laboratory of Colorectal and Pelvic Floor Diseases, The Sixth Affiliated Hospital, Sun Yat-sen University, Guangzhou, China. [3]Biomedical Innovation Center, The Sixth Affiliated Hospital, Sun Yat-sen University, Guangzhou, China. [4]Department of Colorectal Surgery, The First Clinical College of Changsha Medical University, Changsha Medical University, Changsha, China.

L. Kang, L. Huang, and X. Zheng contributed equally as coauthors of this article.

W. Liang, H. Liu, and Z. Zeng were co–senior authors of this article.

Corresponding Authors: Liang Kang, Sixth Affiliated Hospital of Sun Yat-sen University, Guangzhou 510655, China. Phone: 86-203-845-5369; E-mail: kangl@mail.sysu.edu.cn; Liang Huang, huangl75@mail.sysu.edu.cn; and Xiaobin Zheng, zhengxbn@mail3.sysu.edu.cn

Cancer Immunol Res 2023;11:875–94

doi: 10.1158/2326-6066.CIR-22-0814

a promising immunotherapeutic target and an effective marker of immunotherapy reactivity in colorectal cancer.

Materials and Methods

Colorectal cancer patient samples

Frozen, fresh colorectal cancer tissues were obtained from three dMMR and three pMMR cases to analyze transcriptome alterations by RNA-seq as described previously. Twenty paired colorectal cancer samples and normal adjacent tissues (including 10 dMMR and 10 pMMR cases) were used to analyze KRT17 mRNA expression by qRT-PCR (details below). Five paired colorectal cancer samples and normal adjacent tissue (including 5 dMMR and 5 pMMR cases) were used to analyzed KRT17 protein expression by western blot assay (see below). Tumor tissues were collected immediately after surgery. Some tissues were then stored at −80°C with RNAlater solution (Invitrogen). The remaining tissues were directly stored at −80°C. All patients did not undergo either chemotherapy or radiotherapy before surgery. 446 patients with colorectal cancer (224 dMMR and 222 pMMR patients) who received surgery at our hospital provided formalin-fixed, paraffin-embedded (FFPE) colorectal cancer tissue samples. Patients did not receive neoadjuvant chemoradiotherapy, except high-risk stage II and III patients. Clinical parameters were obtained from the patient electronic medical records located in our hospital. All human tissue samples were obtained with written informed consent from donors. Only paraffin sections from 446 patients with colorectal cancer were collected retrospectively. A total of 120 patients were randomly selected from 446 patients to analyze the difference of KRT17 expression in tumor tissue and adjacent normal tissue, including 60 dMMR and pMMR cases. All procedures were carried out in accordance with the declaration of Helsinki and were approved by the Institutional Review Committee of the Sixth Affiliated Hospital of Sun Yat-sen University.

Colorectal cancer patient cohort treated with anti–PD-1

Patient eligibility criteria included pathologic confirmation of colorectal cancer, at least four weeks of prior treatment with the anti–PD-1 drug pembrolizumab, adequate tumor biopsy samples, available baseline patient and disease information, and sufficient archival tissue available for analysis. We collected endoscopic biopsy samples from all included patients with colorectal cancer. All tissues were fixed in formalin and then embedded in paraffin. Clinical, radiographic, and treatment data for each patient were collected retrospectively. All human tissue samples were obtained with written informed consent from donors. All procedures were carried out in accordance with the declaration of Helsinki. A cohort of 30 patients with colorectal cancer receiving pembrolizumab was established in our study, and all patients were histologically diagnosed dMMR cancer, including 15 cases in each of the responder and non-responder groups. The objective clinical response was defined by RECIST version 1.1.

Cell lines and cultures

All human colon cancer cell lines, including DLD1, HCT8, WiDr, Lovo, SW48, HCT116, RKO, HCT15, and HEK293T, were all obtained from the ATCC. The mouse colon cancer cell line CT26 was obtained from the ATCC and the murine colon cancer cell line MC38 was obtained from the National Infrastructure of Cell Line Resource (Beijing, China). DMEM (Gibco, Thermo Fisher Scientific) mixed with 10% FBS (Gibco, Thermo Fisher Scientific) was used to culture all cells in a 5% CO_2 atmosphere. All cell lines were validated by STR DNA finger-printing and the reauthentication took place in 2021. All cell lines were routinely tested for *Mycoplasma*. Cells were generally passaged 1–2 times before being used for subsequent experiments. All cell lines were passaged within 15 times in our study.

Protocols for transfection and lentivirus infection are described previously in the indicated section. After cells were transfected 48 hours with the indicated plasmid, 25-μm MG132 (Sigma-Aldrich) or DMSO (Sigma-Aldrich) was added into medium and cultured 12 hours. For IFNγ stimulation, MC38 and CT26 cells were transfected with *vector* and *Krt17* plasmids with 50 ng/mL IFNγ (NovoProtein) or BSA (Sigma-Aldrich) for 48 hours.

Animal models

BALB/C nude mice (4–5 week), BALB/c mice, and C57BL/6J mice (6–8 weeks) were obtained from VitalRiver Laboratory Animal Technology. All mice were fed in pathogen-free conditions at the Experimental Animal Center of the Sixth Affiliated Hospital of Sun Yat-sen University. For the xenograft tumor model using nude mice, a total of 2×10^5 MC38 or CT26 cells transfected with *vector* or with *Krt17* lentivirus were resuspended in 100 μL of a mixture with PBS and Matrigel (Corning; 1:1) and then subcutaneously inoculated into right flank of each nude mice. For the xenograft tumor model using immune-competent mice, a total of 2×10^5 MC38 cells transfected with *vector* or with *Krt17* lentivirus were subcutaneously inoculated into right flank of each C57BL/6J mouse; a total of 2×10^5 CT26 cells transfected with *vector* or with *Krt17* lentivirus were subcutaneously inoculated into right flank of each BALB/c mouse. For *in vivo* depletion of $CD8^+$ T cells, either MC38 or CT26 tumor-bearing mice were injected intraperitoneally with 200 μg (10 mg/kg) of either anti-CD8 (Bio X Cell) or IgG (Bio X Cell) every four days starting on day 4 after tumor inoculation. For the *in vivo* anti–PD-1 treatment study, either C57BL/6J mice bearing MC38 tumors or BALB/c mice bearing CT26 tumors received intraperitoneal injection with either 200 μg (10 mg/kg) of anti–PD-1 (Bio X Cell) or IgG (Bio X Cell) every three days starting on day 6 after tumor inoculation. For the *in vivo* neutralizing anti-CXCL10 treatment study, BALB/c mice bearing CT26 tumors received intraperitoneal injection with either 40 μg (2 mg/kg) of anti-CXCL10 (RD system) or IgG (RD system) every three days starting on day 15. Tumor volumes were measured on the basis of the following formula: Volume (mm^3) = (long diameter × short diameter^2)/2. Tumor long and short diameters were monitored by caliper, and mice were checked every two days. For tumor growth assays, mice were sacrificed when tumor volume of any one mouse reached 2,000 mm^3 or there was a clear difference in tumor volume between control and experimental groups. For mouse survival analysis, the mouse was sacrificed when its own tumor volume reached 2,000 mm^3 and survival time was calculated from the time after tumor inoculation. Tumor weights were also measured. Tumor tissues were collected and then used in all following experiments. Animal experiments were authorized by the Institutional Animal Care and Use Committee of Sun Yat-sen University and complied with the Guide for the Care and Use of Laboratory Animals of the National Institutes of Health (National Academies Press, 2011) in China.

Tissue dissociations

Tumor tissues obtained from patients with colorectal cancer and mouse models were dissociated to perform extract RNA or protein. For RNA extraction, tumor tissues were removed from the −80°C freezer and were cut into approximately 3-mm pieces on ice with a blade. The tissues were transferred to a new 2-mL Eppendorf tube, and then 4-mm steel balls (Servicebio) and 1-mL TRizol reagent (Invitrogen) were added. A tissue crusher (Qiagen Tissue Lyser LT) was used to

dissociate the tissues with a frequency of 60 Hz, a time of 10 minutes. After tissue dissociations, RNA was extracted (described below). For protein extraction, 500-μL T-PER tissue protein extraction reagent (Thermo Fisher Scientific) was used instead of 1-mL TRizol reagent, and the remaining steps were as described above.

Cell isolations and activation

Spleens were isolated from BALB/c mice or C57BL/6J mice. A 70-μm cell filter (Corning) was placed in a 10-cm cell culture dish (Corning), 6 mL lymphocyte separation solution (BioLegend) was added, and mouse spleens were quickly minted and ground. The lymphocyte separation solution was transferred into 15-mL centrifuge tube (Corning), and 1-mL serum-free DMEM (Gibco) was slowly added into centrifugal tube. Samples were centrifuged at 800 x *g* for 30 minutes at 4°C. The tunica albugnean layer was collected and washed once by adding 5 mL precooled serum-free DMEM (Gibco), and centrifuged at 250 x *g* for 10 minutes at 4°C. Finally, the supernatant was discarded. For cell activation, the isolated cells were cultured in 8 mL DMEM (Gibco) containing 10% FBS (Gibco), 50 U/mL IL2 (MCE), and 200 μL mouse CD3/CD28 dynbeads (Invitrogen) for 48 hours.

m^{6}A-RNA immunoprecipitation assay

Samples used for the m^{6}A-RNA immunoprecipitation (MeRIP) assay included MC38 and CT26 cells, cells treated with 50 ng/mL IFNγ (NovoProtein) or BSA (Sigma-Aldrich), cells transfected with *vector* and *Krt17* plasmids, and/or cells transfected with coexpressing plasmids. Each group contained three biological replicates, and m^{6}A abundance of *Cxcl10* mRNA was evaluated by qRT-PCR. Total RNA was obtained by TRizol Reagent (Invitrogen). 300-ng RNA was retained as an input sample for qRT-PCR (described below), and the residual sample was used for MeRIP. MeRIP was performed by adding residual RNA into 500 μL immunoprecipitation (IP) buffer [10 mmol/L Tris, 150 mmol/L NaCl, 0.1% NP-40 (APE×BIO), 100 U RNase inhibitor (Omega), pH 7.4] and incubated with 4 μg/mL m^{6}A antibody (Abcam). The m^{6}A-IP mixture was incubated for 2 hours at 4°C, and then Dynabeads Protein A (Life Technologies) coated with BSA was added into the m^{6}A-IP mixture and incubated for an additional 2 hours at 4°C. The mixture was then washed in IP buffer and eluted by competition with 50 μg/mL N6-methyladenosine (Santa Cruz Biotechnology). 20-μL RLT buffer (Thermo Fisher Scientific) was used to elute the bound RNA from beads. The ReverTra Qpcr RT Master Mix kit (TOYOBO) was used to reverse-transcribe the extracted IP RNA and input RNA into cDNA library according to its instructions. m^{6}A enrichment of *Cxcl10* was evaluated by qRT-PCR.

qRT-PCR

qRT-PCR samples included human and mouse colon cancer cell lines, whole-tumor tissues of patients with colorectal cancer, and whole-tumor tissues of the xenograft tumor model. Tissues were dissociated before RNA extraction (described above). Total RNA was extracted by TRizol Reagent (Invitrogen). The ReverTra Qpcr RT Master Mix kit (TOYOBO) was used to reverse-transcribe the extracted RNA into cDNA library according to its instructions. The SYBR Green PCR Master Mix (Applied Biosystems) was used to perform qRT-PCR on LightCycler 96 (Roche). According to its instructions, a volume of 10-μL RT-qPCR reaction system was prepared as follows: 5 μL 2X SYBR Green Mix + 0.25 μL PCR Forward Primer (10 μmol/L) + 0.25 μL PCR Reverse Primer (10 μmol/L) + 1 μL cDNA template sample + 3.5 μL ddH2O. Each sample contained three biological replicates. We applied the $2^{-\Delta\Delta CT}$ method and normalized to β-actin to determine gene expression. For MeRIP–qRT-PCR, equal amounts of either IP RNA or input RNA from each sample was extracted for construction of the cDNA library. Reverse transcription and PCR processes are similar to those described above. The relative m^{6}A abundance of *Cxcl10* was measured by its expression levels of MeRIP sample under normalization by its expression levels of input sample. All genes were assessed by qRT-PCR and their primer sequences were shown (Supplementary Tables S1 and S2).

RNA-seq analysis

Using TRizol reagent (Invitrogen), total RNA was isolated from mouse xenograft tumor tissues (MC38 cell line with *vector* and *Krt17* lentivirus) or colorectal cancer tumor tissues (colorectal cancer cases with dMMR and pMMR). For each group, three biological replicates were used. Tissues were dissociated before RNA extraction (described above). RNA purity was examined on a Bioanalyzer 2200 device (Aligent), and the RNA integrity number of all samples ranged from 7 to 9. Ribosomal RNA was then removed using the RiboMinus Eukaryote Kit (Qiagen), and a cDNA library was created by a NEB Next Ultra RNA Library Prep Kit (New England Biolabs). cDNA fragments were purified and end repaired, and a poly(A) tail was added. Finally, using an Illumina HiSeq 3000 (Illumina), deep sequencing was carried out, aligning the clean reads to the reference genome (GRCH37.p13 NCBI). DESeq2 software was used to examine the differences in gene expression between two groups. The genes with the parameter of absolute fold change >2 and FDR < 0.01 were defined differentially expressed genes. qRT-PCR was used to confirm the expression of relevant genes (primer sequences shown in Supplementary Tables S1 and S2).

Plasmid construction, transfection, and lentivirus infection

For KRT17, *Krt17*, *Ythdf2*, *Cxcl10*-expressing plasmids, the full-length ORF sequences with tag of these genes (KRT17 GeneID: 3872, *Krt17* GeneID: 16667, *Ythdf2* GeneID: 213541, *Cxcl10* GeneID: 15945) were, respectively, subcloned into the pcDNA3.1 vector (Thermo Fisher Scientific). The activity of the internal ribosome entry site (IRES) was examined with pCMV-IRES-Renilla Luciferase-IRES-Gateway-Firefly Luciferase (pIRIGF) vector (Hebei Yancheng Biotechnology). Colorectal cancer cells, including DLD1, HCT8, MC38, and CT26 cell lines, were transfected with above vectors using Lipofectamine 3000 (Invitrogen). For construction of shKRT17 plasmids, shKRT17 sequences were cloned into pLKO.1 vector (Hebei Yancheng Biotechnology). All constructs were verified by sequencing. For stable lentivirus infection, HEK293T cells were transfected with the indicated plasmids, psPAX2 and pMD2G (Addgene) according to the manufacturer's instructions. Colorectal cancer cells were then transfected with the above supernatant in the presence of 8 μg/mL polybrene (Beyotime) and selected with puromycin (MCE, China) after infection. For construction of coexpressing cells used in rescue experiments, equal amounts of *Krt17* and *Ythdf2* plasmids or lentivirus were added into the medium, the next steps of transfection or lentivirus infection were consistent with the above steps. The oligonucleotide sequences for vector construction are listed in Supplementary Table S3.

IP assay

The cells transfected with the relevant plasmids were lysed in Pierce IP lysis buffer (Thermo Fisher Scientific) in the presence of a protease inhibitor cocktail (including protease inhibitors and phosphatase inhibitors; Thermo Fisher Scientific) for 30 minutes at 4°C. Centrifugation was conducted on cell lysates at 13,000 x *g* for 20 minutes at 4°C. The antibodies used in IP assays included anti-KRT17 (1:30,

Abcam) and anti-YTHDF2 (1:50, Abcam). Next, the antibodies were applied to the 200-μL Pierce Protein A/G magnetic beads (Thermo Fisher Scientific) for 4 hours at 4°C to crosslink the antibodies. The antibody-crosslinked beads were mixed with the 500-μL cell lysates overnight at 4°C. After being washed with washing buffer (Cayman) five times, the beads were incubated with 2× sample loading buffer (Beyotime) and then boiled for 10 minutes. The lysates were resolved on SDS-PAGE (described below).

Western blotting

Western blotting samples included human and mouse colon cancer cell lines, whole-tumor tissues of patients with colorectal cancer, and whole tumor from the xenograft tumor model. Tissues were dissociated before protein extraction (described above). Total protein was extracted by T-PER tissue protein extraction reagent (Thermo Fisher Scientific). The concentration of protein samples was analyzed with the BCA standard protein kit (Dingguo), and quantitative experiments were carried out on the basis of its instructions. 5× SDS loading buffer (Dingguo) was used. 1–10 μg protein per sample was loaded into gel based on the sample type and primary antibody. The blots were blocked with 5% nonfat milk (Biotopped), and 0.45-μm polyvinylidene difluoride membrane (Millipore) was used to transfer protein from the 10% running gel (Servicebio). Primary antibodies used for western blotting are listed in Supplementary Table S4. The dilution of primary antibodies was in accordance with their instructions. Secondary antibodies of HRP-label IgG included anti-mouse (1:1,000, Servicebio) and anti-rabbit (1:1,000, Servicebio). Mini-PROTEAN Tetra Cell, Mini Trans-Blot Module, PowerPac Basic Power, and ChemiDoc (Bio-Rad) were used. SDS-PAGE Running Buffer Powder, SDS-PAGE Transfer Buffer Powder, TBS powder, and Tween-20 (Servicebio) were used. Blotting for β-actin (1:1,000, Proteintech) was used as a loading control.

Cell proliferation, migration, and invasion assays

DLD1 cells transfected with overexpressed plasmids (vector or KRT17 plasmids) and HCT8 cells transfected with knockdown plasmids (shNC, shKRT17–1, and shKRT17–2 plasmids) were used to determine the effect of KRT17 on colorectal cancer cell phenotypes. Cell proliferation was examined using the proliferation curve and plate colony formation. For the proliferation curve, 6,000 cells were plated into 96-well plates (Corning) with serum-free DMEM (Thermo Fisher Scientific), and cell proliferation was monitored every 10 hours using an IncuCyte Essens Bioscience incubator (Essens Bioscience). For plate colony formation, 600 cells were seeded in 6-well plates (Corning) with serum-free DMEM (Thermo Fisher Scientific) and cultured for 10 days. The colonies were then fixed with 4% paraformaldehyde (Servicebio) and stained with 0.1% crystal violet (Servicebio) for 15 minutes at room temperature. Cell colonies were imaged and counted with inverted microscope (Leica). Cell migration was determined by a wound healing assay. A total of 4×10^6 cells were plated into 6-well plates (Corning) and incubated until confluency was reached. A rectilinear scratch was performed using a 100-μL pipette (Corning) tip. After 24 hours, cells were fixed with 4% paraformaldehyde (Servicebio) for 15 minutes, and then stained with 0.1% crystal violet (Servicebio) for 15 minutes at room temperature. Wound closure was imaged using an inverted microscope (Leica) and ImageJ software (NIH) was used for quantitative analysis. For invasion assays, 24-well plates (Corning) with 8-μm pore size chamber inserts (Corning) were used. A total of 4×10^4 cells were seeded in the upper chamber well with 200 μL serum-free DMEM and 800 μL of DMEM (Thermo Fisher Scientific) with 20% FBS (Thermo Fisher Scientific) was added into the lower chamber. After 48 hours, cells migrating through the membrane were fixed with 4% paraformaldehyde (Servicebio) for 15 minutes, and then stained with 0.1% crystal violet (Servicebio) for 15 minutes. The migrating cells were imaged using an inverted microscope (Leica) and ImageJ software (NIH) was used for quantitative analysis.

Cycloheximide-chase experiments

MC38 or CT26 cells transfected with *vector* or *Krt17* plasmids were used to perform cycloheximide-chase experiments. Using DMEM (Thermo Fisher Scientific) with 10% FBS (Thermo Fisher Scientific), a total of 2×10^5 cells were plated into 6-well plates (Corning). 100 μg/mL cycloheximide (Thermo Fisher Scientific) was added to the medium, and cells were harvested at 0, 2, 4, 6, 8, 10 hours for protein extraction. Western blotting was used to analyze the expression of YTHDF2 protein (described above).

ELISA

For analysis of CXCL10 production, 100 μL supernatant was collected after MC38 and CT26 cells were transfected with indicated plasmid (*vector* and *Krt17* plasmids, coexpressed plasmids, or *vector* and *Cxcl10* plasmids) in presence of 50 ng/mL IFNγ for 48 hours. A RayBio Human or Mouse Cytokine Antibody Array (Raybiotech, Inc.) was used, and a standard curve was performed according to the manufacturer's protocol. The ELISA plate was assessed using an enzyme-label instrument (Thermo Fisher Scientific) with wavelength set at 450 nm. The sample concentration was calculated by substituting the instrument readings into the formula obtained from the standard curve.

IHC and scoring

All samples were FFPE tissues from a cohort of 446 patients with colorectal cancer, a cohort of colorectal cancer treated with pembrolizumab, and animal models described above. Mouse/Rabbit Polymer Test System Universal kit (ZS-bio) was used to perform IHC according to its instructions. Briefly, paraffin sections were routinely dewaxed and hydrated. Citrate solution (Servicebio) was selected and placed in microwave (Midea) on medium-high heat for 8 minutes for antigen repair. The citrate solution was cooled to room temperature naturally. Endogenous peroxidase blocking agents (ZS-bio) were added and incubated for 10 minutes at room temperature. Primary antibodies used for IHC are listed in Supplementary Table S4. After incubation overnight at 4°C, enzyme-labeled anti-goat IgG polymer (ZS-bio) was incubated for 20 minutes at room temperature. Diaminobenzidine solution (ZS-bio) was used to stain at room temperature. Microscopy (Leica) was used to observe staining results and to collect images. Tumor region of human and mouse tumor tissues was assessed for the expression of KRT17, YTHDF2, and CXCL10. The staining scores were quantified on the basis of the staining intensity and proportion of positively stained cells. The proportion of positively stained cells was determined by the percentage of positive stained area using the following four groups: grade 0 = 0, grade 1 = 1% to 25%, grade 2 = 26% to 50%, grade 3 = 51% to 75%, and grade 4 = >75%. The staining intensity was divided into the following four groups: grade 0 with no staining, grade 1 with weak staining, grade 2 with medium staining, and grade 3 with strong staining. The staining scores were calculated using the following formula: Staining scores = staining intensity × proportion of positively stained cells. The expressions of KRT17, YTHDF2, and CXCL10 were determined by the staining scores on a scale from 0 to 12 and divided into low and high groups based on the median. The $CD3^+$ and $CD8^+$ T-cell density per patient was assessed on tumor parenchyma (TP) and invasive margin (IM), which

determined by counting the number of positive cells per tissue sample using tumor tissue sections, as described previously (13). Using similar method, the infiltration level of T lymphocyte on tumor region of mouse tumor tissue was assessed.

Immunofluorescent staining

Mouse MC38 and CT26 cell lines were chosen to evaluate cellular localization of KRT17 and YTHDF2 proteins. A cell slide (Thermo Fisher Scientific) was spread into a well of 12-well plate (Corning), and each well was inoculated with 2×10^4 MC38 or CT26 cells. 4% paraformaldehyde (Servicebio) was used to fix cells for 30 minutes at room temperature. 0.5% Triton X-100 (Servicebio) was added to break cell membrane for 30 minutes at room temperature and 1% BSA (Thermo Fisher Scientific) was used to block for 1 hour at room temperature. Specific primary antibodies, including anti-KRT17 (1:200, Abcam) and anti-YTHDF2 (1:200, Abcam) were incubated with the cells overnight at 4°C. Samples were added with Alexa 488- or 594-conjugated goat antibodies (1:1,000, Thermo Fisher Scientific) against rabbit or mouse IgG. The cells assessed using a confocal laser scanning microscope (Leica TCS-SP8) after being counterstained with DAPI (Merck Millipore).

Actinomycin D assay

For the half-life of mRNA assessment, after MC38 and CT26 cells were transfected with indicated plasmid (*vector* and *Krt17* plasmids, or coexpressed plasmids) with 50 ng/mL IFNγ for 48 hours, gene transcription was blocked by adding 5 mg/mL Actinomycin D (Sigma-Aldrich) to the cells. DMSO was used as a negative control. Cells were harvested at 0, 6, 12, 24 hours and the stability of *Cxcl10* was analyzed by qRT-PCR as described above.

In vitro T-cell migration assays

In a Transwell device with a polycarbonate membrane with an 8-μm pore size (Corning), an *in vitro* migration experiment was performed. The top compartment contained resuspended 2×10^4 activated $CD8^+$ T cells after two washes using sterile PBS (BOSTER), and the bottom chamber contained 1 mL nondiluted conditioned media from MC38 or CT26 cells transfected with indicated plasmids (*vector* and *Krt17* plasmids, co-expressed plasmids, or *vector* and *Cxcl10* plasmids) with 50 ng/mL IFNγ (NovoProtein) for 48 hours. After the coculture for 24 hours, the media of the bottom chamber were collected; it was centrifuged at 13,000 x *g* for 20 minutes at 4°C. After centrifugation, the supernatant was discarded and cells at the bottom of the eppendorf tube were resuspended in 20 μL of PBS. Using Cell counting analyzer (Nexcelom), cell numbers in the bottom chamber were then counted.

RNA immunoprecipitation assay and RNA IP sequencing

The Magna RIP RNA-Binding Protein IP Kit (Merck Millipore) was used to carry out the RNA immunoprecipitation (RIP) assay according to its instructions. For RIP, anti-YTHDF2 (1:1,000, Abcam) was used and included mouse MC38 and CT26 cells, and those transfected with *vector* and *Krt17* plasmids and those transfected with coexpressing plasmids. Equal amounts of either IP RNA or input RNA from each sample was extracted for construction of the cDNA library. Reverse transcription and PCR processes are similar to those described above. The relative expressions of indicated genes (*Cxcl10*, *Ccl2*, and *Ccl7*) were measured by its expression in the RIP sample after normalization of its expression in the input sample. For RIP sequencing (RIP-seq), the mouse MC38 cell line was chosen to extract RNA. For next-generation sequencing (NGS), input RNA and RIP RNA were generated by Geneseed Biotech Company. The TruSeq Stranded mRNA Sample Prep Kit (Illumina) was used for NGS library preparation, a BioAnalyzer High Sensitivity DNA chip (Geneseed Biotech) was used for quantification, and a 19Illumina HiSeq 2500 was used for deep sequencing. Using Bowtie2 version 2.1.0, the reads were first mapped to the most recent UCSC transcript set (14), and RSEM version 1.2.15 was used to assess gene expression. The RSEM approach was used to quantify the RNA-seq reads and RIP-seq reads at the gene level, and they were standardized to fragments per kilobase of exon model per million mapped fragments.

Mass spectrometry

The gel from the IP assay using anti-KRT17 (Abcam) was cut into tiny pieces. Peptides were dispersed in 0.1% formic acid (FA; Thermo Fisher Scientific) and 2% acetonitrile (ACN; Thermo Fisher Scientific) following trypsin digestion (Promega) and then were immediately placed onto a reversed-phase analytical column (Thermo Fisher Scientific). The gradient consists of increasing solvent B (0.1% FA in 80% ACN) from 5% to 50% in 40 minutes, while maintaining a consistent flow rate of 300 nL/min, as recommended by the manufacturer. Using Q Exactive hybrid quadrupole-Orbitrap mass spectrometer (Thermo Fisher Scientific), MS analysis was conducted. Detection model included reflection mode and positive ion spectroscopy, the ion source accelerated voltage was 20 KV, and each peptide map was accumulated by 200 bombardments. Thermo Fisher Scientific's Q Exactive was used to perform tandem mass spectrometry (MS/MS) on the peptides, which was then connected online to perform ultra-performance liquid chromatography. The m/z scan range for MS scans was 350 to 1800 m/z. A fixed initial mass of 100 m/z was chosen. By using Uniprot Aedis Aegypti as a search engine, MASCOT software (Matrix Science) was used to identify proteins.

Statistical analysis

All data are presented as mean ± standard deviation (SD) unless otherwise noted. Data analysis was conducted using SPSS16.0 statistical package (IBM). For continuous variables with normal distributions, a two-tailed Student *t* test or one-way ANOVA was used to establish statistical significance, whereas either Mann–Whitney or Kruskal–Wallis test was applied for skewed distributions. For survival analysis, Kaplan–Meier plots and log-rank tests were used. GraphPad Prism 8 (GraphPad) was used to make ROC curve and analyze AUC. Statistical significance was defined as a P value of 0.05.

Availability of data and materials

The RNA-seq data of colorectal cancer cases with different MMR status used in the study (HRA002906) are available in the GSA-Human public repository. The RNA-seq data of xenograft tumor tissues in mice (CRA007974) are available in GSA. The RIP-seq data in this study were deposited at GSA database with an accession number (CRA007975). The MS data have been stored to the ProteomeXchange Consortium via the PRIDE partner repository (15) with the dataset identifier PXD036433.

Results

High KRT17 expression indicates favorable clinical outcomes in dMMR colorectal cancer

dMMR tumors tend to have massive CTL infiltration in colorectal cancer (11). To uncover specific transcriptomic differences that might influence CTL infiltration, we performed a transcriptomic analysis using three dMMR cases and three pMMR cases (**Fig. 1A**). By analyzing RNA-seq data, we found that the mRNA transcript expression of 159 genes was upregulated and 62 genes were

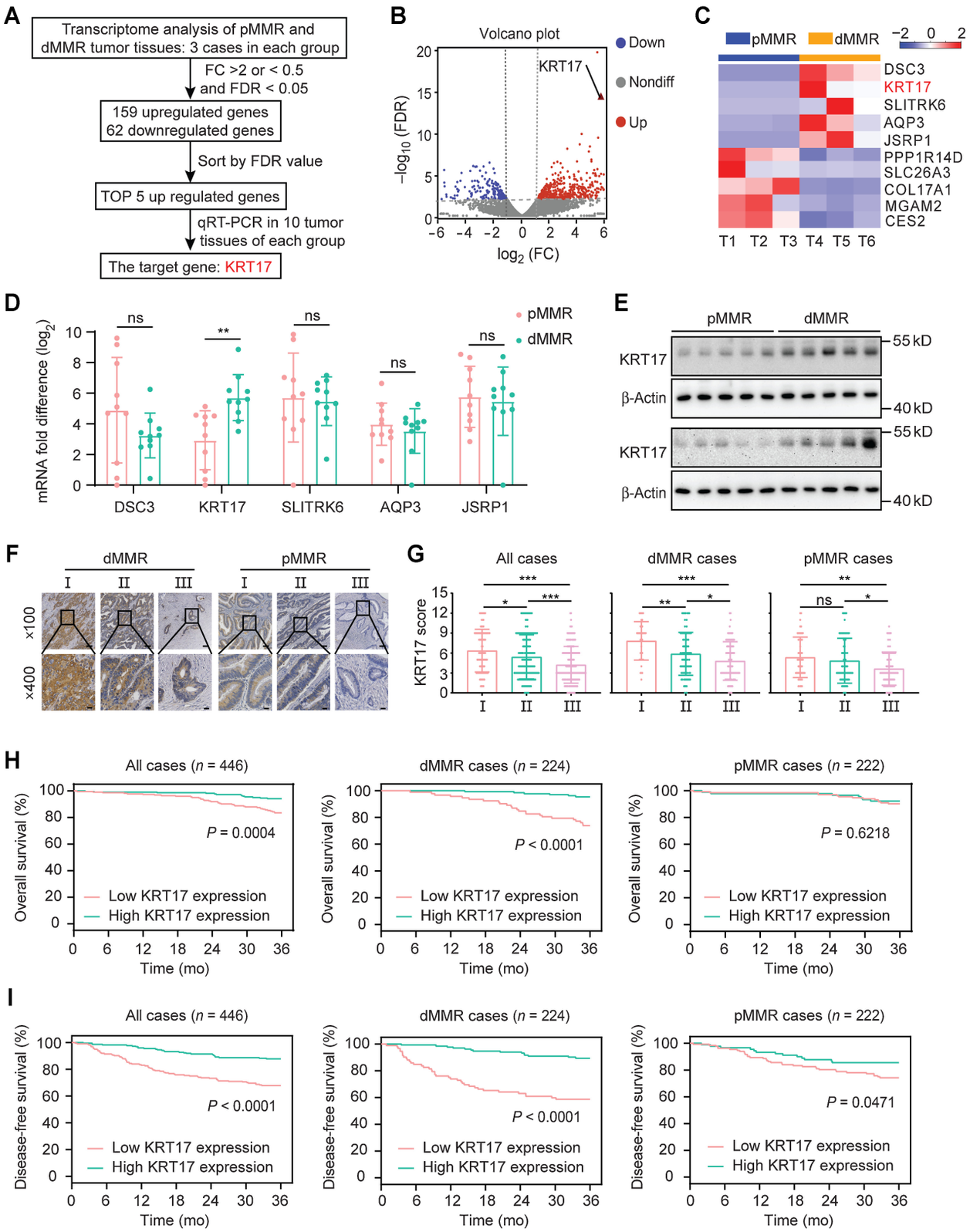
A
Transcriptome analysis of pMMR and dMMR tumor tissues: 3 cases in each group
FC >2 or < 0.5 and FDR < 0.05
159 upregulated genes
62 downregulated genes
Sort by FDR value
TOP 5 up regulated genes
qRT-PCR in 10 tumor tissues of each group
The target gene: KRT17
B
Volcano plot
Down
Nondiff
Up
KRT17
−log10 (FDR)
log2 (FC)
C
pMMR
dMMR
DSC3
KRT17
SLITRK6
AQP3
JSRP1
PPP1R14D
SLC26A3
COL17A1
MGAM2
CES2
T1 T2 T3 T4 T5 T6
D
pMMR
dMMR
mRNA fold difference (log2)
DSC3
KRT17
SLITRK6
AQP3
JSRP1
E
pMMR
dMMR
KRT17
β-Actin
55 kD
40 kD
F
dMMR
pMMR
×100
×400
G
All cases
dMMR cases
pMMR cases
KRT17 score
H
All cases (n = 446)
dMMR cases (n = 224)
pMMR cases (n = 222)
Overall survival (%)
P = 0.0004
P < 0.0001
P = 0.6218
Low KRT17 expression
High KRT17 expression
Time (mo)
I
All cases (n = 446)
dMMR cases (n = 224)
pMMR cases (n = 222)
Disease-free survival (%)
P < 0.0001
P < 0.0001
P = 0.0471
Low KRT17 expression
High KRT17 expression
Time (mo)

downregulated in dMMR tumors compared with pMMR tumors (**Fig. 1B**). The expression of the top 5 upregulated genes was then detected in each group of 10 colorectal cancer tissues using qRT-PCR. These results suggested only KRT17 (keratin, type I cytoskeletal 17) was differentially expressed between dMMR and pMMR tumor tissues (**Fig. 1C** and **D**). Moreover, mRNA expression was also detected in 20 paired tissues and showed KRT17 expression was higher in tumor tissues compared with normal tissues (Supplementary Fig. S1A). A similar association was found in stratified analyses of patients with dMMR or pMMR status (Supplementary Fig. S1A). Western blots confirmed that protein expression of KRT17 was higher in dMMR colorectal cancer tissues than pMMR colorectal cancer tissues (**Fig. 1E**). Similarly, Western blot analysis of 10 paired colorectal cancer samples and normal adjacent tissues showed KRT17 was highly expressed in tumor tissues (Supplementary Fig. S1B).

To explore clinical characteristics of KRT17 expression, IHC was used to examine KRT17 expression in 446 colorectal cancer cases, including 224 dMMR and 222 pMMR cases (**Fig. 1F**). In all colorectal cancer samples, KRT17 expression gradually decreased in more advanced TNM stages (**Fig. 1G**). Similar results were found in our subsequent stratified analyses of patients with dMMR or pMMR status (**Fig. 1G**). In addition, we analyzed 120 paired tumor tissues, including 60 (each) dMMR and pMMR cases, which suggested that KRT17 expression in tumor tissues was higher than in corresponding normal adjacent tissues (Supplementary Fig. S1C and S1D). Kaplan–Meier curves showed that higher KRT17 expression associated with better overall survival [OS; log-rank test, $P = 0.0004$; hazard ratio (HR), 0.3345; 95% confidence interval (CI), 0.1921–0.5824] and disease-free survival (DFS) in all cases (log-rank test, $P < 0.0001$; HR, 0.3287; 95% CI, 0.2214–0.4878; **Fig. 1H** and **I**). Stratification of the cohort into patients with dMMR ($n = 224$) or pMMR ($n = 222$) found that high KRT17 expression associated with good OS in dMMR cases (log-rank test, $P < 0.0001$; HR, 0.1536; 95% CI, 0.0735–0.3210), but not in pMMR cases (log-rank test, $P > 0.05$; **Fig. 1H**). However, patients with high KRT17 expression had less recurrence at 3 years, regardless of MMR status (dMMR: log-rank test, $P < 0.0001$; HR, 0.2018; 95% CI, 0.1143–0.3562; pMMR: log-rank test, $P = 0.0471$; HR, 0.5292; 95% CI, 0.2965–0.9446; **Fig. 1I**). These data indicate a potential interplay between KRT17 expression and MMR status in tumor cells, which affects the prognosis of patients with colorectal cancer.

KRT17 suppresses tumor growth by increasing CTL infiltration into tumors

On the basis of the better prognosis of patients with colorectal cancer with high KRT17 expression, we considered whether KRT17 expression affected tumor growth. In all colorectal cancer samples, there was no significant correlation between KRT17 expression and proliferating tumor cells. Similar results were also found in dMMR and pMMR cases (Supplementary Fig. S1E). To further determine whether KRT17 affected colon cancer phenotypes, we tested KRT17 expression in human colorectal cancer cell lines by qRT-PCR (Supplementary Fig. S2A). The DLD1 cell line had the lowest KRT17 expression, thus we chose these cells for overexpression. Because of the weak migratory ability of the HT29 and WiDr cell lines (16), we chose the cells with the third highest KRT17 expression for knockdown. The efficacy of overexpression and knockdown in the two colorectal cancer cell lines was validated using qRT-PCR (Supplementary Fig. S2B) and Western blot (Supplementary Fig. S2C) assays. Next, the proliferation curve showed that neither overexpression nor knockdown of KRT17 changed cell growth (Supplementary Fig. S2D). Similarly, the colony formation assay indicated that either overexpression or knockdown of KRT17 did not affect the number and size colonies following a 10-day incubation (Supplementary Fig. S2E). In addition, neither the migratory nor invasive activities were not changed by either KRT17 overexpression or knockdown (Supplementary Fig. S2F and S2G). These results suggested that KRT17 had no effect on colon cancer phenotypes *in vitro*.

On the basis of the distinct difference of TME between dMMR and pMMR colorectal cancers, we assumed that KRT17 expression in tumor cells would affect tumor progression by changing the immune TME. To explore the effect of KRT17 on immune TME in tumors of different MMR status, we chose the MC38 and CT26 mouse colorectal cancer cell lines. Next, we constructed MC38 and CT26 with stable overexpression of *Krt17* (Supplementary Fig. S2H and S2I) and subcutaneously inoculated into immune-deficient nude mice. The results indicated that *Krt17* had no effect on the tumor growth in immune-deficient nude mice *in vivo* (Supplementary Fig. S2J and S2M). We next subcutaneously inoculated the two cell lines with or without stable *Krt17* overexpression into immune-competent mice. Both MC38 and CT26 tumors with *Krt17* overexpression were substantially smaller than tumors from *vector* cells (**Fig. 2A**). Consistently, the tumors from the *Krt17* overexpression group showed decreased weight compared with tumors from the *vector* group (**Fig. 2B** and **C**). These results indicated that KRT17 inhibited tumor growth in immune-competent mice.

To fully understand the gene changes occurring in TME with *Krt17* overexpression, we next conducted RNA-seq to investigate specific transcriptomic alterations of tumor tissues from tumor models. Transcriptomic analysis revealed that *Krt17* overexpression in xenograft tumors resulted in significant alterations, including the upregulation of 136 genes and downregulation of 156 genes (**Fig. 2D**). Among the differentially expressed genes in tumors with *Krt17* overexpression, we found increased expression of cytokines and cytotoxic molecules (e.g., *IFNg, Cxcl11, Gzma, Cd2*, and *H2Aa*). Gene oncology analysis was subsequently performed on these differentially expressed genes, and enriched pathways were found to be primarily associated with the immune system process, T-cell activation, chemotaxis, cytokine production, response to cytokine, and lymphocyte homeostasis (**Fig. 2E**). The expression of both IFNγ and granzyme B, two key markers of T lymphocytes, was consistently higher in the *Krt17* overexpression

Figure 1.

High KRT17 expression indicates favorable clinical outcomes in dMMR colorectal cancer. **A,** Schematic showing the screening schedule to find out the key role of KRT17 on transcriptome analysis using three dMMR and pMMR cases. **B,** Volcano plot of different expressed genes obtained by DEseq2 analysis in dMMR tumor tissues compared with pMMR tumor tissues. 159 significantly upregulated or 62 downregulated genes are plotted in red and blue points. **C,** Heat map of the top five up- or downregulated genes screened in dMMR and pMMR tumor tissues. **D,** qRT-PCR analysis of top five upregulated genes in 10 (each) dMMR and pMMR tumor tissues. **E,** Western blot analysis of KRT17 protein expression in 10 dMMR and pMMR tumor tissues. **F,** Immunostaining of KRT17 in the tumor in a representative human colorectal cancer case of different clinical grade with dMMR compared with a pMMR case; scale bars, 100 μm (top), 20 μm (bottom). **G,** Quantification of KRT17 expression by IHC score in all 446 human colorectal cancer samples. **H** and **I,** Kaplan–Meier survival curve of patients with colorectal cancer layered by the KRT17 expression in tumor tissue sections. Values are represented as mean ± SD. *, $P < 0.05$; **, $P < 0.01$; ***, $P < 0.001$; ns (no significance), by two-tailed Student *t* test (**D**), one-way ANOVA (**G**) or log-rank test (**H** and **I**).

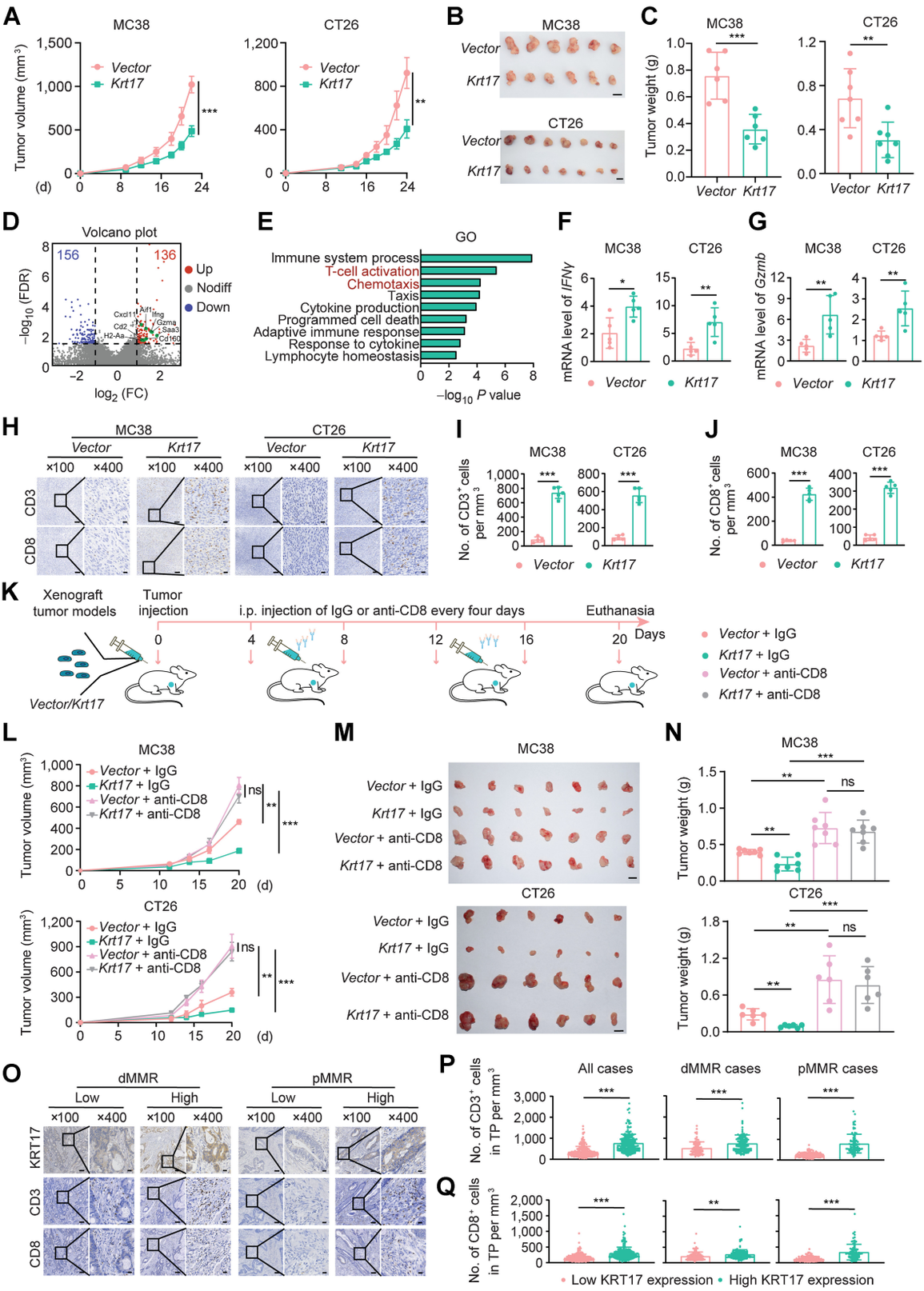
A
MC38
CT26
Tumor volume (mm³)
Vector
Krt17
(d)
B
MC38
CT26
Vector
Krt17
C
MC38
CT26
Tumor weight (g)
Vector
Krt17
D
Volcano plot
156
136
Up
Nodiff
Down
−log10 (FDR)
log2 (FC)
E
GO
Immune system process
T-cell activation
Chemotaxis
Taxis
Cytokine production
Programmed cell death
Adaptive immune response
Response to cytokine
Lymphocyte homeostasis
−log10 P value
F
MC38
CT26
mRNA level of IFNγ
G
MC38
CT26
mRNA level of Gzmb
H
MC38
CT26
Vector
Krt17
×100
×400
CD3
CD8
I
MC38
CT26
No. of CD3⁺ cells per mm³
J
MC38
CT26
No. of CD8⁺ cells per mm³
K
Xenograft tumor models
Tumor injection
i.p. injection of IgG or anti-CD8 every four days
Euthanasia
Days
Vector/Krt17
Vector + IgG
Krt17 + IgG
Vector + anti-CD8
Krt17 + anti-CD8
L
MC38
CT26
Tumor volume (mm³)
Ins
(d)
M
MC38
CT26
N
MC38
CT26
Tumor weight (g)
ns
O
dMMR
pMMR
Low
High
KRT17
CD3
CD8
P
All cases
dMMR cases
pMMR cases
No. of CD3⁺ cells in TP per mm³
Q
No. of CD8⁺ cells in TP per mm³
Low KRT17 expression
High KRT17 expression

group than in the *vector* group in the subcutaneous MC38 and CT26 models (**Fig. 2F** and **G**). Taken together, these data suggested that KRT17 played a key role in T-lymphocyte responses.

To further verify these results, we then examined the presence of CTLs in tumor tissue of xenograft tumor models. IHC was used to determine CTL infiltration as indicated by $CD3^+$ and $CD8^+$ T cells (**Fig. 2H**). These results indicated that there were significantly more $CD3^+$ and $CD8^+$ T cells in tumor tissues from the *Krt17* overexpression group than in those from the *vector* group (**Fig. 2I** and **J**). Given that KRT17 appeared to have an inhibitory effect on tumorigenesis, we also investigated the potential contribution of $CD8^+$ T cells to the observed decline in tumor growth using anti-CD8 in the xenograft tumor models (**Fig. 2K**). Treatment with anti-CD8 led to significantly faster tumor growth compared with the IgG control group. Moreover, there was no difference in either tumor volume or tumor weight between *vector* and *Krt17* overexpression tumors in the anti-CD8 group (**Fig. 2L–N**). This demonstrated the indispensable role of CTL responses on KRT17-mediated effects on tumorigenesis.

KRT17 positively correlates with T-lymphocyte infiltration

To verify the potential association between KRT17 expression and T-lymphocyte infiltration in colorectal cancer, we assessed T-lymphocyte infiltration in 446 colorectal cancer samples, including 224 dMMR and 222 pMMR cases. We examined $CD3^+$ and $CD8^+$ cells in two tumor regions: The TP and IM as stated in previous research (11). Regardless of MMR status, both $CD3^+$ and $CD8^+$ cells in the TP were more abundant in high KRT17 expression tumors than those with low KRT17 expression (**Fig. 2O–Q**).

To further demonstrate the effect of KRT17 expression and CTL infiltration in the TP on prognosis, we performed stratified analyses of the cohort. We divided the cohort into two groups based on the median number of $CD3^+$ and $CD8^+$ cells in TP. Among patients with low number of $CD3^+$ cells in TP, high KRT17 expression associated with good OS and DFS in dMMR cases, but not in all cases and pMMR cases (Supplementary Fig. S3A). However, among patients with high $CD3^+$ cells in the TP, those with higher KRT17 expression had better OS and DFS in all cases and dMMR cases, but not in pMMR cases (Supplementary Fig. S3B). Survival and recurrence in all cases was stratified by KRT17 expression regardless of the number of $CD8^+$ cells in the TP, and similar results were shown in dMMR cases but not in pMMR cases (Supplementary Fig. S3C and S3D). In addition, tumors with high KRT17 expression had more $CD3^+$ and $CD8^+$ cells in the IM than those with low KRT17 expression (Supplementary Fig. S4A and S4C). Stratification of the cohort into patients with different number of $CD3^+$ and $CD8^+$ cells in the IM found results similar to those in the TP (Supplementary Fig. S4D–S4G). Collectively, these observations suggested that KRT17 had a protective role in tumor progression by upregulating CTL infiltration in colorectal cancer.

KRT17 facilitates proteolytic degradation of YTHDF2 via ubiquitination

To elucidate the molecular mechanism behind KRT17-mediated regulation of the immune system process, we next performed a co-IP experiment using anti-KRT17 in conjunction with MS to uncover KRT17-interacting proteins. 10 immune-related proteins were found to bind to the KRT17 protein, among which YTHDF2 ranked first according to their respective protein scores (Supplementary Fig. S5A). The two peptide sequences for the YTHDF2 protein were identified by MS (**Fig. 3A**). We then performed reciprocal co-IP experiments and confirmed that KRT17 bound to YTHDF2 (**Fig. 3B**). Subsequent immunofluorescence assays indicated that this interaction may take place in the cytoplasm (**Fig. 3C**).

To further explore function of KRT17 binding, we tested the expression of YTHDF2 in *Krt17*-overexpressing cells. We found that the abundance of *Ythdf2* mRNA level did not change with *Krt17* overexpression *in vitro* and *in vivo* (**Fig. 3D** and **E**). However, YTHDF2 protein levels were decreased under *Krt17* overexpression *in vitro* and *in vivo* (**Fig. 3F** and **G**). Because PSMB8 and SMAD3 have been reported to function in T-lymphocyte homeostasis (17, 18), we tested the effect of *Krt17* overexpression on their protein expression. The results indicated that *Krt17* overexpression did not change the protein level of PSMB8 and SMAD3 (Supplementary Fig. S5B). Thus, these results indicated that *Krt17* overexpression inhibited YTHDF2 protein levels. To further verify the clinical correlation between KRT17 and YTHDF2 protein expressions in colorectal cancer cases, we assessed 446 colorectal cancer cases using IHC to analyze the expression of these two proteins (**Fig. 3H**). YTHDF2 protein expression negatively correlated with KRT17 protein expression in all cases, and a subgroup analysis showed similar results in dMMR and pMMR cases (**Fig. 3I**).

To confirm that KRT17 decreased the protein stability of YTHDF2, we designed a cycloheximide-chase experiment using tumor cells transfected with *vector* or *Krt17*. The YTHDF2 protein level was tested every two hours after cycloheximide treatment by Western blot assays. These results indicated that *Krt17* overexpression lessened the half-life of the YTHDF2 protein (**Fig. 3J**). We also found that the effect of KRT17 on YTHDF2 protein levels could be inhibited by MG132, a proteasome inhibitor (**Fig. 3K**). Collectively, these results suggested that KRT17 induced the proteolytic degradation of YTHDF2. Consistent with these results, we also revealed that KRT17 fully enhanced

Figure 2.

KRT17 suppresses tumor growth by increasing CTL infiltration into tumors. **A,** Average growth curves of subcutaneous xenograft tumors in immune-competent mice after inoculation of MC38 or CT26 cells with *vector* or with *Krt17* lentivirus. MC38, $n = 6$. CT26, $n = 7$. **B** and **C,** Representative pictures and tumors weight of xenograft tumors in immune-competent mice after inoculation of MC38 or CT26 cells with *vector* or with *Krt17* lentivirus. **B,** Scale bars, 1 cm. **D,** Volcano plot of different expressed genes obtained by DEseq2 analysis in xenograft tumor tissues of MC38 with *Krt17* lentivirus compared with the tumor tissues with *vector* lentivirus. 136 significantly upregulated or 156 downregulated genes are plotted in red and blue points. **E,** Meta-enrichment analysis summary for 292 significantly coregulated genes. **F** and **G,** qPCR analysis of *IFNγ* or *Gzmb* expression in the indicated tumors of xenograft tumor models; $n = 5$. **H,** Representative IHC staining of CD3 and CD8 in sections of mouse tumor tissues from the *vector* and *Krt17* overexpression groups; scale bars, 100 μm (left), 20 μm (right). **I** and **J,** Quantification of $CD3^+$ and $CD8^+$ T lymphocytes in mouse tumor tissues; $n = 5$. **K,** Mice were given IgG or anti-CD8 antibody starting on the fourth day after tumor inoculation and treated on the indicated days for a total of 4 treatment. **L,** Tumor growth in mice bearing *vector* and *Krt17* overexpression tumors treated IgG or anti-CD8 antibody. MC38, $n = 7$ (top). CT26, $n = 6$ (bottom). **M** and **N,** Representative pictures and tumors weight of xenograft tumors in mice after inoculation of MC38 or CT26 cells with *vector* or with *Krt17* lentivirus along with IgG or anti-CD8 antibody treatment. **M,** Scale bars, 1 cm. **O,** Immunostaining of KRT17, CD3, and CD8 in the tumor in a representative human colorectal cancer case of different KRT17 expression with dMMR compared with a pMMR case; scale bars, 100 μm (left), 20 μm (right). **P** and **Q,** Quantification of $CD3^+$ and $CD8^+$ T lymphocytes in TP in all 446 human colorectal cancer samples, including 224 dMMR colorectal cancer samples and 222 pMMR samples. Values are represented as mean ± SD except for (**A**); **I**, mean ± SEM. TP, tumor parenchyma. *, $P < 0.05$; **, $P < 0.01$; ***, $P < 0.001$; ns, no significance, by two-tailed Student *t* test (**C, F, G, I, J, P**, and **Q**), one-way ANOVA (**A** and **N**) or two-way ANOVA (**L**).

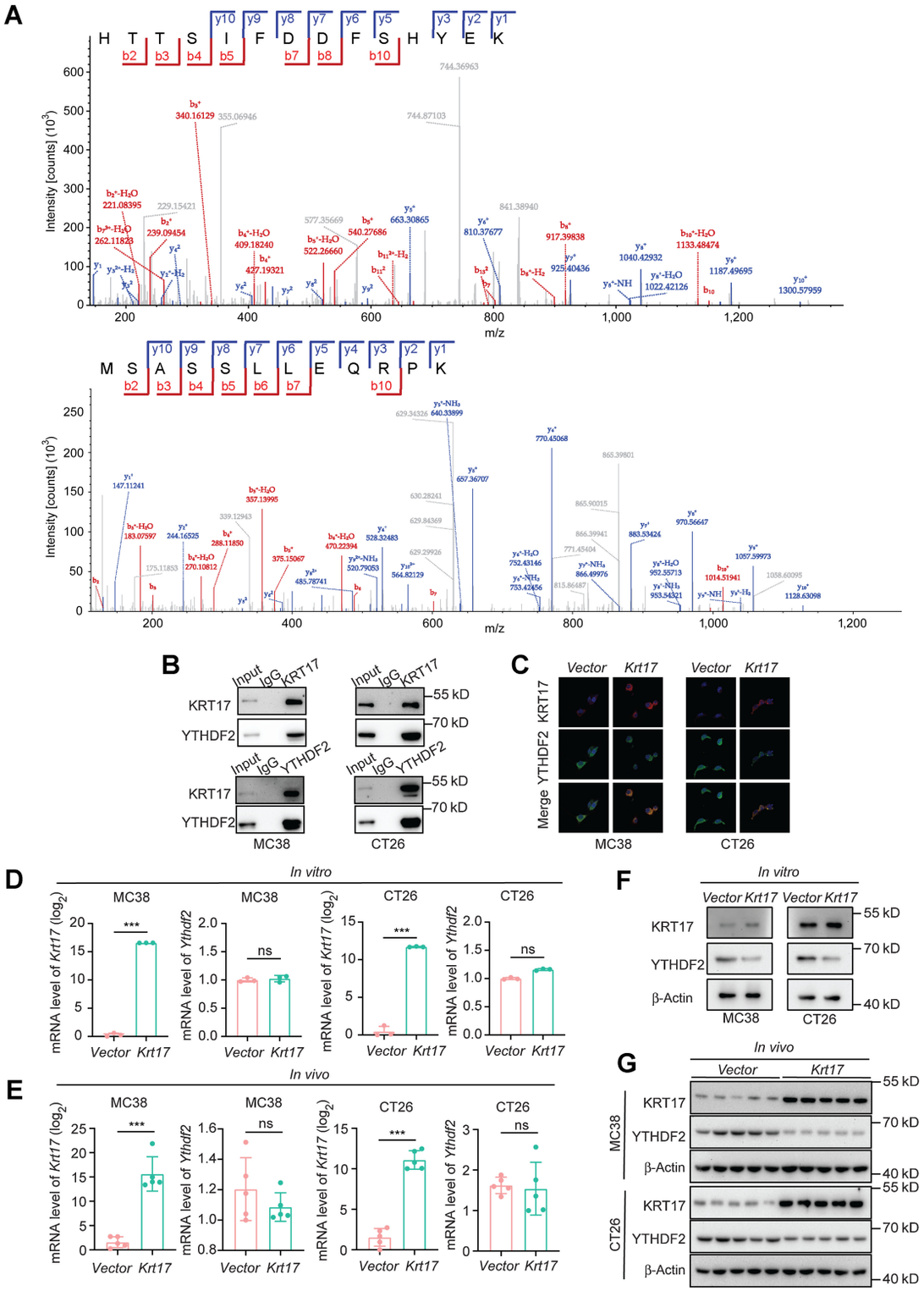

Figure 3.

KRT17 facilitates proteolytic degradation of YTHDF2 via ubiquitination. **A,** The identified YTHDF2 amino acids in immunoprecipitation (IP) products by mass spectrometry. **B,** Western blot analysis of IP using anti-KRT17 or anti-YTHDF2 antibody in MC38 and CT26 cells with indicated antibodies. **C,** Immunofluorescent staining of KRT17 and YTHDF2 in MC38 and CT26 cells transfected with *vector* and *Krt17*. **D,** qRT-PCR analysis of *Krt17* and *Ythdf2* expressions in MC38 and CT26 cells transfected with *vector* and *Krt17*. **E,** qRT-PCR analysis of *Krt17* and *Ythdf2* expressions in xenograft tumor tissue from the *vector* and *Krt17* overexpression groups. **F,** Western blot analysis of KRT17 and YTHDF2 expressions in MC38 and CT26 cells transfected with *vector* and *Krt17*. **G,** Western blot analysis of KRT17 and YTHDF2 expressions in xenograft tumor tissue from the *vector* and *Krt17* overexpression groups. (*Continued on the following page.*)

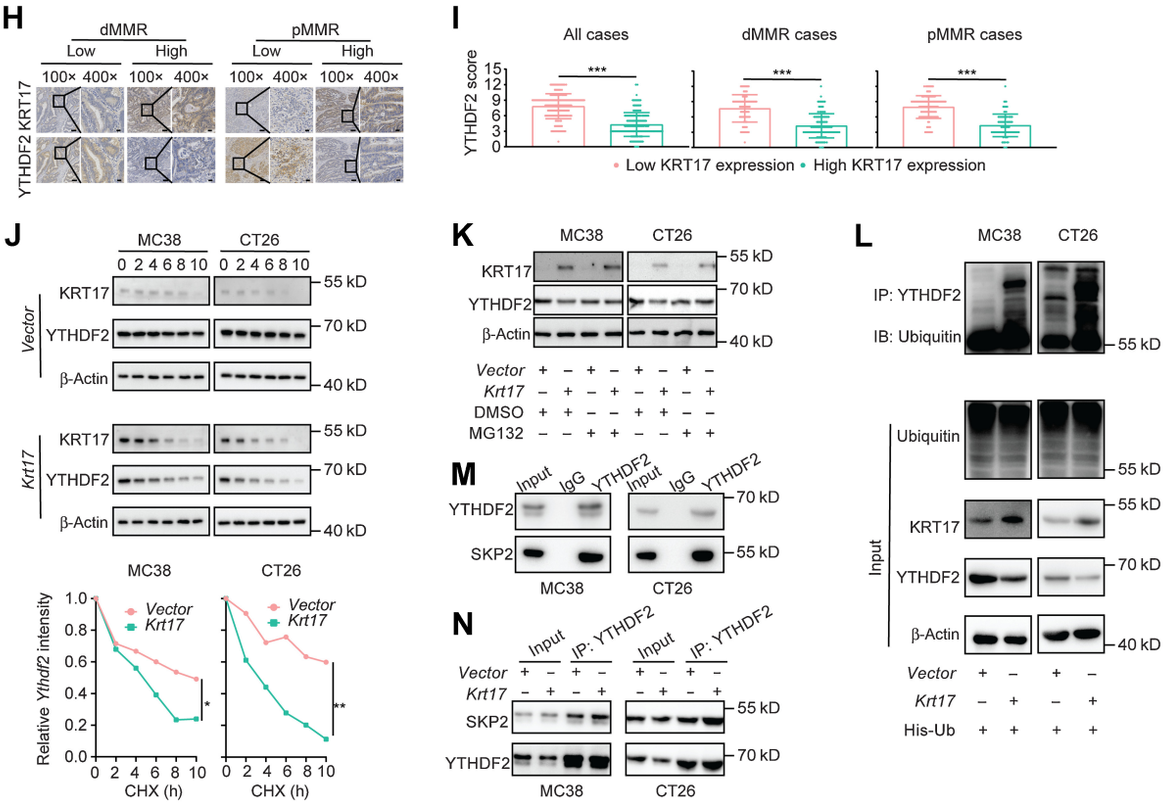

Figure 3.

(*Continued.*) **H,** Immunostaining of KRT17 and YTHDF2 in the tumor in a representative human colorectal cancer case of different KRT17 expression with dMMR compared with a pMMR case; scale bars, 100 μm (left), 20 μm (right). **I,** Quantification of KRT17 and YTHDF2 expressions in all 446 human colorectal cancer samples, including 224 dMMR colorectal cancer samples and 222 pMMR samples. **J,** Western blot analysis of KRT17 and YTHDF2 protein levels in MC38 or CT26 cells transfected with *vector* or *Krt17* with cycloheximide (CHX, 100 μg/mL) treatment at the indicated time. The quantification of YTHDF2 expression is shown in the bottom. **K,** Western blot analysis of KRT17 and YTHDF2 protein levels in MC38 and CT26 cells transfected with *vector* or *Krt17* with MG132 (25 μm) for 12 hours. **L,** Western blot analysis of YTHDF2 ubiquitin levels after IP using anti-YTHDF2 antibody in MC38 and CT26 cells transfected with the indicated plasmids. **M,** Western blot analysis of IP using anti-YTHDF2 antibody in MC38 and CT26 cells with indicated antibodies. **N,** Western blot analysis of IP using anti-YTHDF2 antibody in MC38 and CT26 cells transfected with *vector* or *Krt17* plasmids. Values are represented as mean ± SD. *, $P < 0.05$; **, $P < 0.01$; ***, $P < 0.001$; ns (no significance), by two-tailed Student *t* test (**D, E,** and **I**), one-way ANOVA (**J**).

YTHDF2 ubiquitination in both MC38 and CT26 cells (**Fig. 3L**). It has been reported that S-phase kinase–associated protein 2 (SKP2), which acts as the substrate recognition component of E3 ubiquitin ligase complexes, binds to YTHDF2 and prompts YTHDF2 proteolysis by the CRL–NEDD8 pathway (19). Therefore, we investigated whether KRT17 promoted YTHDF2 ubiquitination through the CRL–NEDD8 pathway. Co-IP assays verified that YTHDF2 bound to SKP2 in both MC38 and CT26 cells (**Fig. 3M**). Moreover, the interaction between YTHDF2 and SKP2 was stronger in *Krt17*-overexpressing cells than in *vector* cells (**Fig. 3N**). In summary, these results suggested that KRT17 prompted ubiquitination-mediated degradation of the YTHDF2 protein in colorectal cancer.

Ythdf2 overexpression blocks the immunomodulatory effect of KRT17

YTHDF2 has reported to be an oncogene in several cancers, including lung cancer (20), ovarian cancer (21), and acute myelogenous leukemia (22). However, the role of YTHDF2 in colorectal cancer still remains poorly understood. Therefore, IHC was conducted to analyze YTHDF2 expression levels in 446 colorectal cancer cases, including 224 dMMR and 222 pMMR cases (Supplementary Fig. S5C). YTHDF2 expression gradually increased with more advanced TNM stages in all cases, and subgroup analyses of patients with either dMMR or pMMR status also had similar results (Supplementary Fig. S5D). Notably, patients with high YTHDF2 expression had worse OS (log-rank test, $P < 0.0004$; HR, 3.540; 95% CI, 2.019–6.206) and DFS in all cases (log-rank test, $P < 0.0001$; HR, 3.244; 95% CI, 2.171–4.847; Supplementary Fig. S5E and S5F). Stratification of the cohort showed that higher YTHDF2 expression associated with worse OS in dMMR cases (log-rank test, $P < 0.0001$; HR, 7.440; 95% CI, 3.513–15.76), but not in pMMR cases (log-rank test, $P > 0.05$; Supplementary Fig. S5D). However, patients with higher YTHDF2 expression had higher recurrence at 3 years, regardless of MMR status (dMMR: log-rank test, $P < 0.0001$; HR, 4.024; 95% CI, 2.265–7.146; pMMR: log-rank test, $P = 0.0013$; HR, 2.679; 95% CI, 1.510–4.751; Supplementary Fig. S5E). These data suggested that YTHDF2 likely function as an oncogene in colorectal cancer.

To explore whether KRT17 affected the immune environment in colorectal cancer by prompting degradation of YTHDF2, we first generated mouse colorectal cancer cell lines with stable overexpression of *Ythdf2* (**Fig. 4A** and **B**). Next, we also confirmed that KRT17-mediated suppression of tumors growth was dependent on YTHDF2,

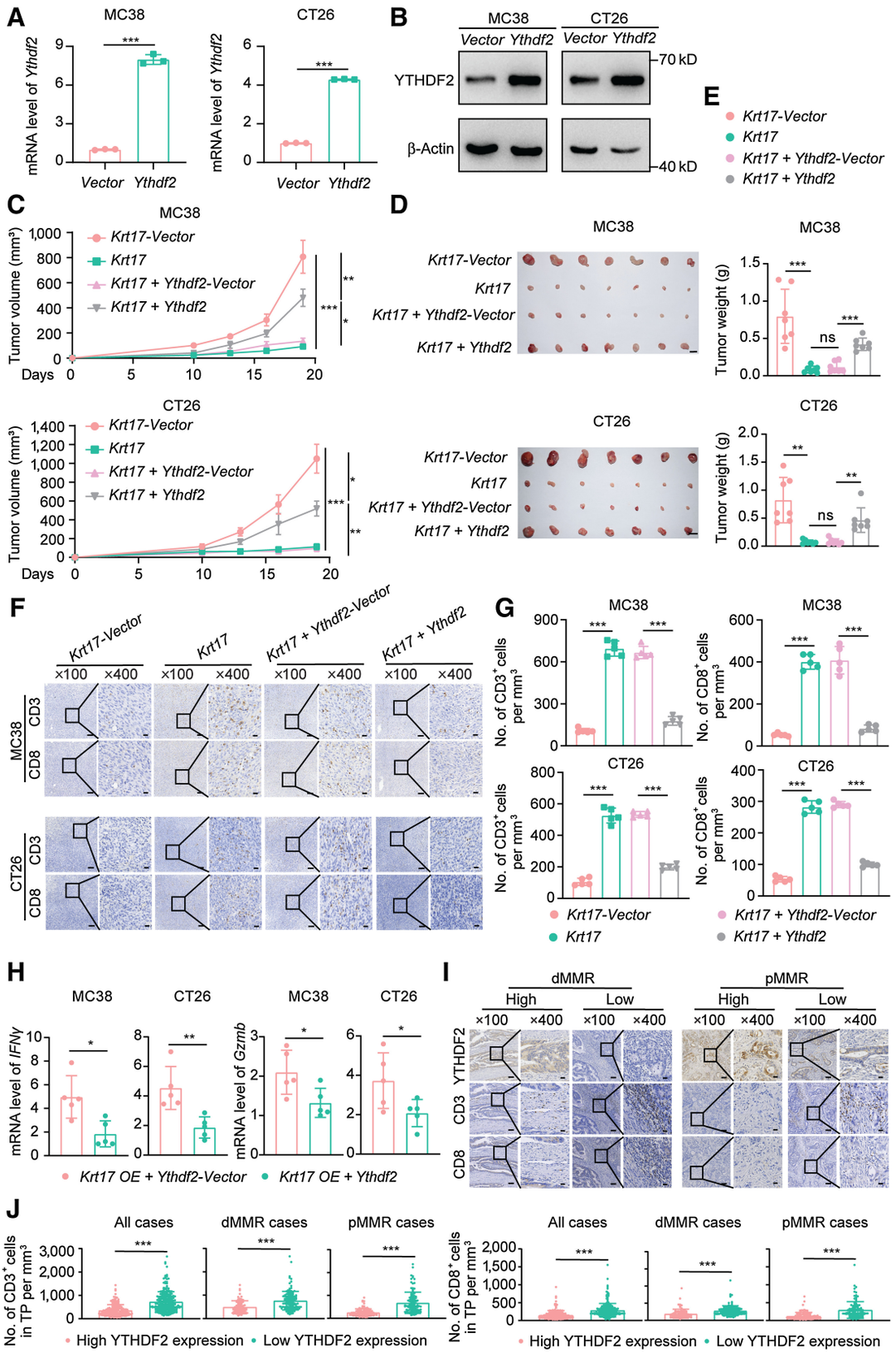
A
MC38
CT26
mRNA level of Ythdf2
Vector Ythdf2
B
MC38 CT26
Vector Ythdf2 Vector Ythdf2
YTHDF2
β-Actin
70 kD
40 kD
E
Krt17-Vector
Krt17
Krt17 + Ythdf2-Vector
Krt17 + Ythdf2
C
MC38
Tumor volume (mm³)
Days
CT26
D
MC38
CT26
Tumor weight (g)
ns
F
×100 ×400
MC38 CD3
MC38 CD8
CT26 CD3
CT26 CD8
G
No. of CD3⁺ cells per mm³
No. of CD8⁺ cells per mm³
H
mRNA level of IFNγ
mRNA level of Gzmb
Krt17 OE + Ythdf2-Vector
Krt17 OE + Ythdf2
I
dMMR
pMMR
High
Low
YTHDF2
CD3
CD8
J
All cases
dMMR cases
pMMR cases
No. of CD3⁺ cells in TP per mm³
No. of CD8⁺ cells in TP per mm³
High YTHDF2 expression
Low YTHDF2 expression

as *Ythdf2* overexpression partially impaired the effect of *Krt17* overexpression on tumor growth (**Fig. 4C** and **E**). Moreover, overexpression of both *Ythdf2* and *Krt17* decreased CTL infiltration compared with only *Krt17* overexpression (**Fig. 4F** and **G**). Consistently, *Ythdf2* overexpression decreased both IFNγ and granzyme B expressions (**Fig. 4H**). These results confirmed that the immunomodulatory effect of *Krt17* overexpression was dependent on YTHDF2 degradation.

We further verified the interaction between YTHDF2 expression and T-lymphocyte infiltration in our colorectal cancer cohort of 446 patients (**Fig. 4I**). Patients with higher YTHDF2 expression had less CTL infiltration in the TP in all cases; similar results were found after stratification of the cohort by MMR status (**Fig. 4J**). Survival and recurrence in all cases was stratified by YTHDF2 expression, regardless of different number of $CD3^+$ and $CD8^+$ T cells in the TP; similar results were shown in dMMR cases but not in pMMR cases (Supplementary Fig. S6A–S6D). In addition, tumors with higher YTHDF2 expression had less $CD3^+$ and $CD8^+$ T cells in the IM than those with low KRT17 expression (Supplementary Fig. S7A–S7C). Stratification of the cohort into patients with different number of $CD3^+$ and $CD8^+$ T cells in the IM found results similar to those in the TP (Supplementary Fig. S7D and S7G). These findings suggested that YTHDF2 had an apparent impact in tumorigenesis by inhibiting adaptive immune responses. In summary, *Ythdf2* overexpression abolished the effects of KRT17 on adaptive immune responses.

CXCL10 is a target of YTHDF2

YTHDF2 has been shown to facilitate the decay of the m^6A-modified transcripts (23). To explore which genes YTHDF2 protein could bind to, we performed high-throughput RIP-seq using anti-YTHDF2. We found that 151 genes bound by YTHDF2 overlapped with upregulated genes in *Krt17* overexpression tumors and 14 immune-related genes between these overlapped (**Fig. 5A**). Among these genes, *Ccl2*, *Ccl7*, and *Cxcl10* have previously been reported to promote lymphocyte migration (24). We performed RIP assays to validate our RIP-seq results and found that CXCL10 was bound to YTHDF2 (**Fig. 5B**).

Next, to investigate whether CXCL10 was modified with m^6A methylation, we performed MeRIP assays using an m^6A antibody. These results showed that *Cxcl10* was methylated in both MC38 and CT26 cells (**Fig. 5C**). In addition, we found that *Cxcl10* was upregulated in *Krt17*-overexpressing tumors compared with control tumors from two xenograft tumor models (**Fig. 5D**). However, *Krt17* overexpression did not change the expression of *Cxcl10 in vitro* (**Fig. 5E**). CXCL10 is one of the IFNγ-stimulated genes (ISG), and previous studies have reported that the presence of IFNγ is necessary for immune regulation of m^6A modification (25). Given this, we reasoned that CXCL10 was regulated by KRT17 when IFNγ was present. Transcriptional analysis of *Krt17*-overexpressing and *vector* cells in the presence of IFNγ suggested enhanced expression of *Cxcl10* (**Fig. 5G**). CXCL10 promoted T-lymphocyte migration, which increased IFNγ expression (**Fig. 2F** and **G**). This finding was consistent with gene set enrichment analysis for responses to IFNγ in *Krt17*-overexpressing tumors showed increased IFNγ-related changes compared with control tumors (**Fig. 5F**).

Previous work has reported that IFNγ increases m^6A modification (26). Thus, we assumed that IFNγ also increased the m^6A levels of CXCL10. We performed MeRIP assays, which showed that IFNγ indeed increased the m^6A levels of CXCL10 (**Fig. 5H**). We also showed that *Krt17* overexpression increased m^6A levels of CXCL10 with IFNγ stimulation (**Fig. 5I**). To ascertain whether the elevated mRNA of *Cxcl10* in *Krt17*-overexpressing tumors was the result of increased mRNA stability, we next evaluated the half-life of *Cxcl10* mRNAs. *Vector* and *Krt17*-overexpressing cells in the presence of IFNγ were administered actinomycin D for 0, 6, 12, and 24 hours. Results demonstrated that *Krt17*-overexpressing cells resulted in more stabilized *Cxcl10* mRNAs than *vector* cells (**Fig. 5J**).

Rescue assays were conducted to confirm whether YTHDF2 was indispensable for KRT17-induced immune regulation. *In vitro*, *Ythdf2* overexpression in *Krt17*-overexpressing MC38 and CT26 cells significantly decreased *Cxcl10* expression in the presence of IFNγ (Supplementary Fig. S8A). To further verify the immune regulation of *Krt17* overexpression dependence on m^6A manner, we performed MeRIP assays. Results showed that *Ythdf2* overexpression in *Krt17*-overexpressing cells decreased m^6A-modified transcripts for *Cxcl10* (Supplementary Fig. S8B). In addition, we assessed *Cxcl10* expression in tumor tissues obtained from xenograft tumor models. Results showed that *Cxcl10* was downregulated in *Ythdf2*-overexpressing tumors compared with control tumors (Supplementary Fig. S8C). Consistently, the analysis of mRNA stability revealed that *Ythdf2*-overexpressing cells significantly decreased stabilized *Cxcl10* mRNAs relative to control cells (Supplementary Fig. S8D).

We analyzed the *Cxcl10* in the supernatant from tumor cells transfected with the indicated plasmid by ELISA. The results showed that *Krt17* overexpression increased CXCL10 in the supernatant, and *Ythdf2* overexpression lessened the enhanced CXCL10 from *Krt17* overexpression (Supplementary Fig. S8E and S8F). To directly verify T-lymphocyte regulation of KRT17, we next performed an *in vitro* migration experiment (**Fig. 5K**), which showed that the migratory ability of T cells was significantly improved following *Krt17* overexpression. Moreover, *Ythdf2* overexpression abolished this ability (**Fig. 5L**). Thus, we concluded that KRT17 regulated CXCL10 expression dependence on YTHDF2. In addition, we found that *Cxcl10* expression had same effect as *Krt17* overexpression (Supplementary Fig. S8G–S8M). There was more T-lymphocyte infiltration in tumor tissues from the *Cxcl10* expression group than in those from the *vector* group (Supplementary Fig. S8N and S8O). In addition, *Cxcl10*

Figure 4.

Ythdf2 overexpression blocks the immunomodulatory effect of KRT17. **A,** qRT-PCR analysis of *Ythdf2* expression in *Ythdf2* overexpression MC38 or CT26 cells. **B,** Western blot analysis of YTHDF2 expression in *Ythdf2* overexpression MC38 or CT26 cells. **C,** Average growth curves of subcutaneous xenograft tumors in immune-competent mice after inoculation of MC38 or CT26 cells with indicated lentivirus ($n = 7$). **D** and **E,** Representative pictures and tumors weight of xenograft tumors in immune-competent mice after inoculation of MC38 or CT26 cells with indicated lentivirus. **D,** Scale bars, 1 cm. **F,** Representative IHC staining of CD3 and CD8 in sections of mouse tumor tissues from the four group; scale bars, 100 μm (left), 20 μm (right). **G,** Quantification of $CD3^+$ and $CD8^+$ T lymphocytes in mouse tumor tissues ($n = 5$). **H,** qPCR analysis of *IFNγ* or *Gzmb* expression in the indicated tumors of xenograft tumor models ($n = 5$). **I,** Immunostaining of YTHDF2, CD3, and CD8 in the tumor in a representative human colorectal cancer case of different YTHDF2 expression with dMMR compared with a pMMR case; scale bars, 100 μm (left), 20 μm (right). **J,** Quantification of YTHDF2 expression, $CD3^+$ and $CD8^+$ T lymphocytes in the tumor in all 446 human colorectal cancer samples, including 224 dMMR colorectal cancer samples and 222 pMMR samples. Values are represented as mean ± SD except for **C** (mean ± SEM). TP, tumor parenchyma. *, $P < 0.05$; **, $P < 0.01$; ***, $P < 0.001$; ns (no significance); by two-tailed Student *t* test (**A**, **H,** and **J**), one-way ANOVA (**E** and **G**) or two-way ANOVA (**C**).

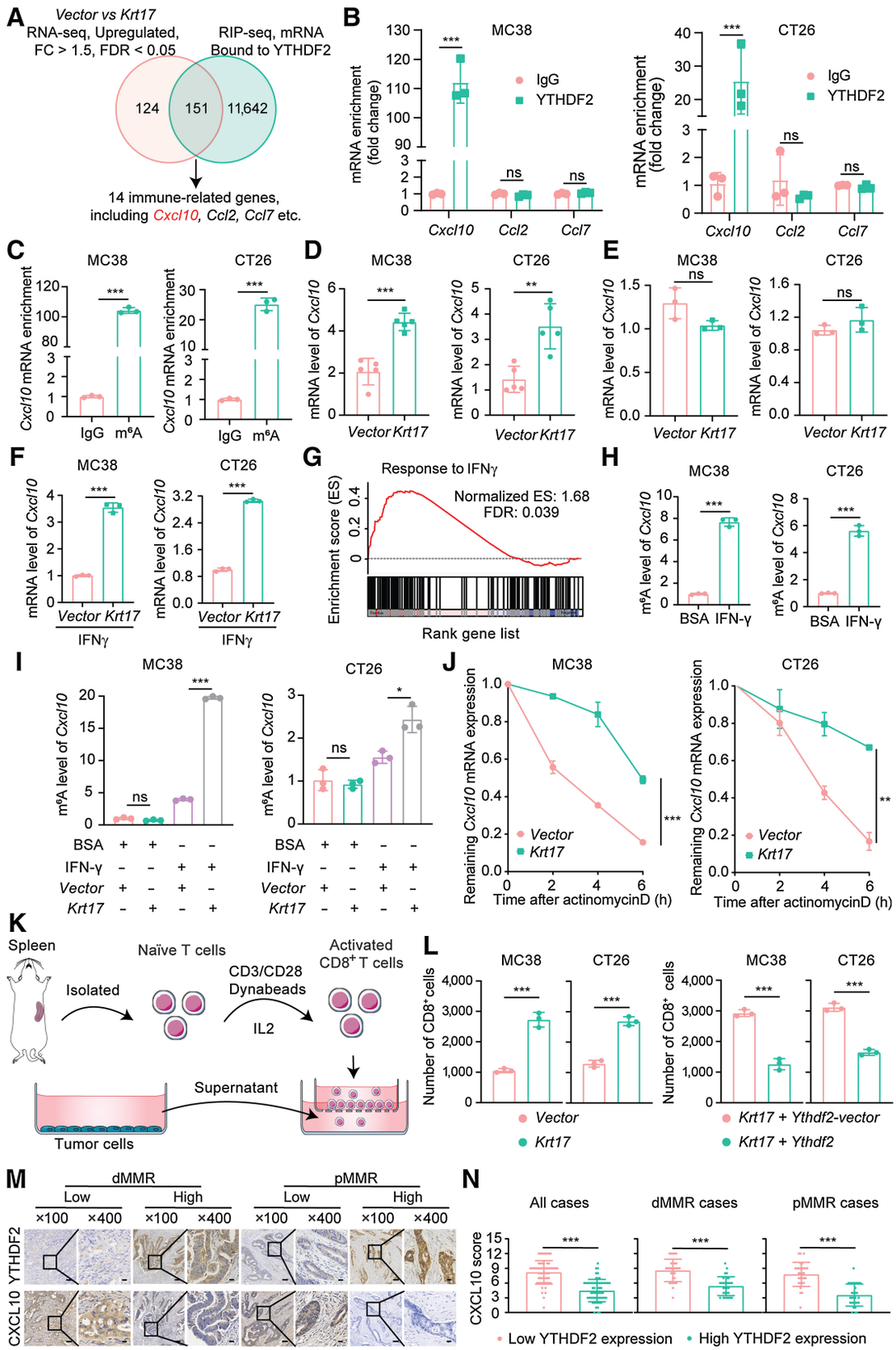
A
Vector vs Krt17
RNA-seq, Upregulated,
FC > 1.5, FDR < 0.05
RIP-seq, mRNA
Bound to YTHDF2
124
151
11,642
14 immune-related genes,
including Cxcl10, Ccl2, Ccl7 etc.
B
MC38
CT26
IgG
YTHDF2
mRNA enrichment (fold change)
Cxcl10
Ccl2
Ccl7
ns
C
MC38
CT26
Cxcl10 mRNA enrichment
IgG
m⁶A
D
MC38
CT26
mRNA level of Cxcl10
Vector Krt17
E
MC38
CT26
mRNA level of Cxcl10
Vector Krt17
F
MC38
CT26
mRNA level of Cxcl10
Vector Krt17
IFNγ
G
Response to IFNγ
Normalized ES: 1.68
FDR: 0.039
Enrichment score (ES)
Rank gene list
H
MC38
CT26
m⁶A level of Cxcl10
BSA
IFN-γ
I
MC38
CT26
m⁶A level of Cxcl10
BSA
IFN-γ
Vector
Krt17
J
MC38
CT26
Remaining Cxcl10 mRNA expression
Vector
Krt17
Time after actinomycinD (h)
K
Spleen
Naïve T cells
Isolated
CD3/CD28
Dynabeads
IL2
Activated
CD8⁺ T cells
Supernatant
Tumor cells
L
MC38
CT26
Number of CD8⁺cells
Vector
Krt17
Krt17 + Ythdf2-vector
Krt17 + Ythdf2
M
dMMR
pMMR
Low
High
×100
×400
YTHDF2
CXCL10
N
All cases
dMMR cases
pMMR cases
CXCL10 score
Low YTHDF2 expression
High YTHDF2 expression

overexpression promoted *IFNγ* and *Gzmb* expressions (Supplementary Fig. S8P). Therefore, *Cxcl10* overexpression was sufficient to inhibit tumor progression by increasing T-lymphocyte infiltration. To explore the correlation between YTHDF2 and CXCL10 expressions in colorectal cancer tissues, IHC was used to analyze YTHDF2 and CXCL10 protein expressions in 120 colorectal cancer samples, including 60 (each) dMMR and pMMR cases (**Fig. 5M**). These results suggested that CXCL10 expression negatively correlated with YTHDF2 expression in all cases and that a similar correlation was found in dMMR and pMMR cases (**Fig. 5N**). A correlation between CXCL10 and KRT17 expressions was also analyzed and suggested that CXCL10 expression positively correlated with KRT17 expression (Supplementary Fig. S8Q). Together, these results identified the KRT17–YTHDF2–CXCL10 axis as a regulator of T-lymphocyte migration in colorectal cancer tumors and suggested that *Krt17* overexpression could be a viable new strategy for immunotherapy treatments.

KRT17 sensitizes colorectal tumors to immunotherapy

Less CTL infiltration is the most recognized cause of resistance to ICIs (27). Therefore, we hypothesized that KRT17 may be involved in the sensitivity of colorectal cancer to immunotherapy. Thus, we designed a treatment schedule to determine whether *Krt17* overexpression influenced immunotherapy responses (**Fig. 6A**). We first treated C57BL/6 bearing MC38 colorectal tumors with anti–PD-1 or isotype control IgG. Anti–PD-1 had a modest effect on tumor growth compared with control IgG antibody treatment (**Fig. 6B**). In addition, mice bearing *Krt17*-overexpressing tumors had slower tumor growth and prolonged survival (**Fig. 6B** and **C**).

Because of pMMR tumors having resistance to ICIs, we further used BALB/c mice bearing CT26 colorectal tumors with anti–PD-1 or isotype control IgG. Inconsistent with our previous MC38 results, mice bearing CT26 showed a more limited effect of anti–PD-1 treatment compared with control IgG (**Fig. 6D**). CT26 tumors with *Krt17* overexpression had apparently shrunk, and BALB/c mice bearing tumors had prolonged survival (**Fig. 6D** and **E**). These findings were similar with C57BL/6 mice bearing *Krt17*-overexpressing MC38 colorectal tumors with anti–PD-1 treatment. To confirm that CXCL10 was responsible for the enhanced immunotherapy response with KRT17, neutralizing CXCL10 antibody was used in the *Krt17* overexpression model with anti–PD-1 treatment. Mice treated with neutralizing CXCL10 antibody had significantly increased tumor growth compared with those with IgG treatment (Supplementary Fig. S9A–S9C). In summary, these findings showed a generalizable role of Krt17 in immunotherapy responses of colorectal tumors.

Colorectal cancer tumors with high KRT17 expression exhibit a favorable response to anti–PD-1 therapy

To determine whether the above findings were translatable to human patients with patients with colorectal cancer, we retrospectively collected 30 colorectal cancer samples obtained from endoscopic biopsy. These patients had all received anti–PD-1 treatment at our hospital. Before PD-1 treatment, all patients were histologically diagnosed with dMMR colorectal cancer. We first examined KRT17 expression via IHC analysis in tumor tissue. Results showed higher KRT17 expression in tumors from responders compared with those who did not respond to anti–PD-1 therapy (**Fig. 6F** and **G**). Similarly, patients with high CXCL10 expression had a better response to pembrolizumab (Supplementary Fig. S9D). Moreover, there was a positive correlation between KRT17 and CXCL10 expressions (Supplementary Fig. S9E).

We next identified whether preexisting $CD3^+$ and $CD8^+$ T cells represented critical factors in the clinical response to PD-1 therapy. Because TP and invasive tumor margin were difficult to define in our endoscopic biopsy samples, we only counted $CD3^+$ and $CD8^+$ cells in the entire field of vision. The response group showed more CTL infiltration than the nonresponse group (**Fig. 6H** and **I**). We further explored the correlation between KRT17 expression and T-lymphocyte density in the endoscopic biopsy samples, and results showed a positive correlation (Supplementary Fig. S9F–S9H). ROC and AUC values suggested that KRT17 expression had better predictive ability than either $CD3^+$ or $CD8^+$ density in tumor tissues of endoscopic biopsy (**Fig. 6J**; Supplementary Fig. S9I and S9J), which might be a promising clinical marker for immunotherapy in colorectal cancer. In summary, KRT17 was highly expressed in immunotherapy responders and had a better predictive performance than CTL density when determining the potential sensitivity to immunotherapy based on endoscopic biopsy samples.

Discussion

Managing the immunosuppressive TME has been identified as a promising therapeutic approach to treat a variety of malignancies. Urgent solutions are needed address limited immunotherapy efficacy in pMMR and partly in dMMR colorectal cancer owing to reduced CTL infiltration (27, 28). The major novel findings of our study provide novel insights on enhancing T-lymphocyte infiltration to reverse immune escape in colorectal cancer (**Fig. 6K**). We found that dMMR tumors had higher expression of KRT17 relative to pMMR tumors, resulting in increased CTL infiltration. This in turn inhibited malignant progression and sensitized colorectal tumors to immunotherapy. Mechanistically, KRT17 mediated the

Figure 5.

CXCL10 is one of the target genes of YTHDF2. **A,** Venn diagram showing the screening schema to find out the target gene of YTHDF2 by RNA-seq of xenograft tumor tissues and RIP-seq using anti-YTHDF2 antibody. **B,** qRT-PCR analysis of RIP using anti-YTHDF2 antibody in MC38 and CT26 cells. **C,** qRT-PCR analysis of MeRIP using m^6A antibody in MC38 and CT26 cells. **D,** qPCR analysis of *Cxcl10* expression in the indicated tumors of xenograft tumor models ($n = 5$). **E,** qPCR analysis of *Cxcl10* expression in MC38 and CT26 transfected with *vector* or *Krt17* plasmids. **F,** qRT-PCR analysis of *Cxcl10* expression in MC38 and CT26 cells transfected with *vector* and *Krt17* plasmids with IFNγ (50 ng/mL) for 48 hours. **G,** Gene set enrichment analysis to assess specific enrichment of response of IFNγ in xenograft tumor tissues of MC38 with *Krt17* lentivirus or with *vector* lentivirus. **H,** qRT-PCR analysis of MeRIP using m^6A antibody in MC38 and CT26 with IFNγ (50 ng/mL) for 48 hours. **I,** qRT-PCR analysis of MeRIP using m^6A antibody in MC38 and CT26 transfected with *vector* or *Krt17* plasmids with BSA or IFNγ (50 ng/mL) for 48 hours. **J,** mRNA stability of *Cxcl10* by qRT-PCR in MC38 and CT26 cells transfected with *vector* or *Krt17* plasmids with stimulation of IFNγ. **K,** Schematic diagram of $CD8^+$ T-cell migration assays. **L,** Quantification of $CD8^+$ T cells passing through the membrane of a Transwell system. **M,** Immunostaining of YTHDF2 and CXCL10 in the tumor in a representative human colorectal cancer case of different KRT17 expression with dMMR compared with a pMMR case; scale bars, 100 μm (left), 20 μm (right). **N,** Quantification of YTHDF2 and CXCL10 expressions in 120 human colorectal cancer samples, including 60 dMMR colorectal cancer samples and 60 pMMR samples. Values are represented as mean ± SD. MeRIP, m^6A-RNA IP. *, $P < 0.05$; **, $P < 0.01$; ***, $P < 0.001$; ns (no significance), by two-tailed Student *t* test (**B–I, L,** and **N**), one-way ANOVA (**J**).

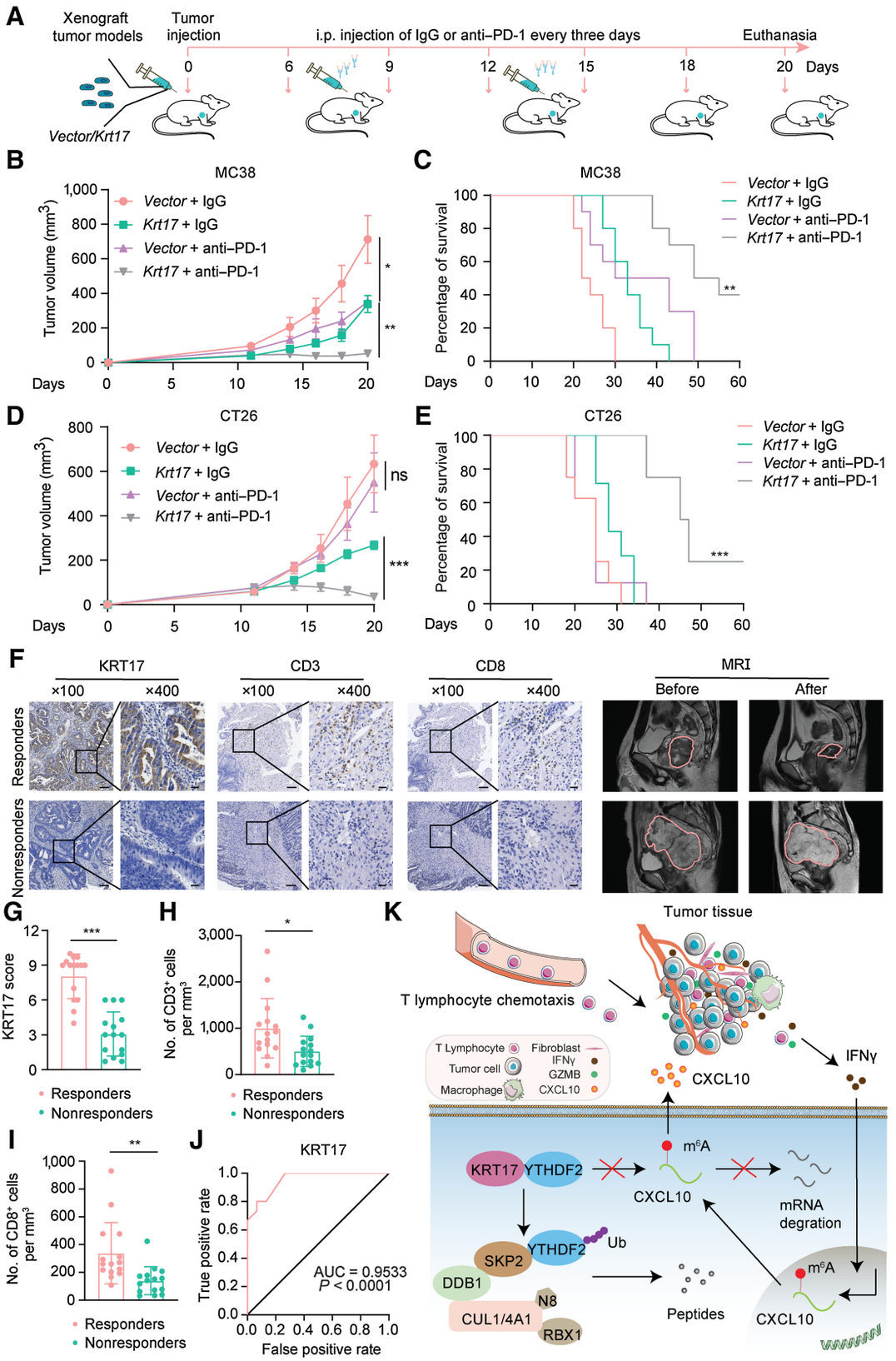
A
Xenograft tumor models
Tumor injection
i.p. injection of IgG or anti–PD-1 every three days
Euthanasia
0
6
9
12
15
18
20
Days
Vector/Krt17
B
MC38
Tumor volume (mm3)
Vector + IgG
Krt17 + IgG
Vector + anti–PD-1
Krt17 + anti–PD-1
Days
C
MC38
Percentage of survival
D
CT26
ns
***
E
CT26
F
KRT17
CD3
CD8
MRI
×100
×400
Before
After
Responders
Nonresponders
G
KRT17 score
H
No. of CD3+ cells per mm3
I
No. of CD8+ cells per mm3
J
KRT17
True positive rate
False positive rate
AUC = 0.9533
P < 0.0001
K
Tumor tissue
T lymphocyte chemotaxis
T Lymphocyte
Tumor cell
Macrophage
Fibroblast
IFNγ
GZMB
CXCL10
IFNγ
CXCL10
KRT17
YTHDF2
m6A
mRNA degration
SKP2
Ub
DDB1
CUL1/4A1
N8
RBX1
Peptides

proteolytic degradation of YTHDF2, which increased *Cxcl10* mRNA expression by inhibiting degradation of m^{6}A-modified transcripts. CTL infiltration increased with CXCL10 expression. On the basis of our combined *in vivo* and *in vitro* observations, the role of the KRT17–YTHDF2–CXCL10 axis was identified in patients with colorectal cancer with pMMR. This finding reinforces the clinical significance of our discovery. The observed connections between KRT17 and CTL infiltrations will also contribute to a better understanding of how KRT17 influences colorectal cancer etiology and may provide additional insights into prospective treatment options for treating pMMR tumors.

The mechanisms underlying the relationship between MMR status and a high CTL microenvironment in colorectal cancer remain largely unknown. The MMR system functions to remove DNA base mismatches, which mainly arise during either DNA replication or DNA damage. Status of dMMR specifically refers to mutations in four genes MSH2, MLH1, PMS2, and/or MSH6 that lose the ability to clear DNA base mismatches. As a result, these DNA base mismatches lead to the production of many mutation-related proteins. Therefore, one important factor may be the increased number of tumor neoantigens generated by high mutational load in dMMR tumors (29, 30). Mutated neoantigens are tumor-specific and may not induce immune tolerance (31). However, there were few studies exploring other mechanisms besides neo-antigenicity. As shown in the previous studies, the concordance rate between RNA-seq and qRT-PCR experiments varied from approximately 16% to 80% (32, 33). In this study, we found that 20% (1/5) genes identified by RNA-seq were validated in a greater number of samples by qRT-PCR. The results appeared to be consistent with previous reports (32, 33). In our studies, we demonstrated a regulatory mechanism for T-lymphocyte homeostasis in colorectal cancer. Specifically, *Krt17* overexpression promoted T-lymphocyte migration into the TP and invasive tumor margin by increasing the production of the classical lymphocyte chemokine CXCL10. This may provide new theoretical guidance for understanding the immune regulation of different MMR states.

Our discoveries also offer proof for a tumor-suppressive role of KRT17. However, preceding studies have revealed conflicting findings regarding the influence of KRT17 on tumor malignancy progression. For instance, KRT17 is upregulated in cervical, oral squamous cell carcinoma, and gastric cancer, and KRT17 is a poor prognostic biomarker in these cancers (34–36). In contrast, the protective role of KRT17 on tumor development has been supported by paired high-resolution lineage information with single-cell RNA-seq. These findings were further validated using CRISPR-based perturbations (37). Moreover, it has been reported that KRT17 affects skin tumorigenesis through an immunoregulatory mechanism involving many pathways, such as: (i) changed chemokine expression profile from Th2 polarization to Th1/Th17 signature (38); (ii) interaction with RNA-binding protein hnRNP K, thus regulating the expression of CXCR3 ligands CXCL9, CXCL10, CXCL11, and other chemokine genes (39); (iii) co-localization with a transcriptional regulator AIRE and bound to NF-κB consensus sequence at the promotor regions of pro-inflammatory genes (40). This suggests that the common immunoregulatory mechanism of KRT17 is to regulate the formation of a pro-inflammatory immune microenvironment in skin tumorigenesis. However, KRT17 has been reported to promote immune escape and ICIs resistance in head and neck cancer (41). Our findings demonstrated that KRT17 was highly expressed in dMMR tumors and prompted ubiquitination-mediated proteolytic degradation of YTHDF2. Ultimately, this increased CXCL10 expression and attracted T lymphocytes into the tumor. This disagreement may be caused by the functional differences of KRT17 in different tumor types, and more studies are needed to clarify the functional diversity of KRT17.

YTHDF2 is an m^{6}A modification reader that promotes rapid decay of m^{6}A-modified transcripts (23). Emerging evidence has demonstrated that YTHDF2 has significant effects on immune regulation and cytokine production (42). For instance, Wu and colleagues show that YTHDF2 increases the decay of KDM6B to promote H3K27me3 methylation of proinflammatory cytokines, which then decrease their expression (43). Depletion of *Ythdf2* in tumor cells elevates the transcription of both Stat1 and Irf1 in the presence of IFNγ, thus increasing the induction of ISGs and sensitizing tumors to immunotherapy (25). Our research here also offers evidence for an immune escape role of YTHDF2. We showed that overexpression of *Ythdf2* inhibited T-lymphocyte migration by decay of m^{6}A-modified transcript of *Cxcl10* with IFNγ stimulation, thereby promoting malignant phenotypes in colorectal cancer. The finding that overexpression of *Ythdf2* partially attenuated the *Krt17* overexpression phenotype suggests that other mechanisms may be in play. KRT17 has been reported to regulate target proteins through multiple pathways, including nucleus localization (40), nuclear export (39), and phosphorylation (44). *Krt17* overexpression did not affect the protein level of PSMB8 and SMAD3, so other mechanisms or other molecules downstream require further exploration in the future. Various targets of YTHDF2 have been reported in cancer, including CEBPA, SOCS2, PD-1, CXCR4, and SOX10 (22, 26, 45). We identified CXCL10 as a key target of YTHDF2 that functions in an m^{6}A-dependent manner to regulate the lymphocyte migration in colorectal cancer. Overall, these findings mechanistically provide the physiological role of the KRT17–YTHDF2 cascade in driving tumor-infiltrating lymphocyte migration and could provide a new immunotherapeutic strategy in colorectal cancer.

Recent research has revealed an important role for epigenomic reprogramming in tumor cells for tumor evasion. It has been shown that the histone modulator EZH2 modulates the transcription of the chemokines CXCL9 and CXCL10 by regulating DNMT1-mediated DNA methylation to prevent T-cell migration into tumors (46, 47). Depletion of the epigenetic regulator PBAF complex promotes chromatin accessibility to enhance tumor response to T-lymphocyte

Figure 6.

KRT17 sensitizes colorectal cancer to immunotherapy. **A,** Schematic diagram of anti–PD-1 treatment models given IgG or anti–PD-1 antibody starting on the sixth day after tumor inoculation and treated on the indicated days for a total of 5 treatment. **B** and **D,** Tumor growth in mice bearing *vector* and *Krt17* overexpression tumors treated IgG or anti–PD-1 antibody. $n = 8$. **C** and **E,** Survival of mice in each group. **F,** Immunostaining of KRT17, CD3, and CD8 in sections of tumor tissues by endoscopic biopsy and representative picture of MRI from the colorectal cancer responders and nonresponders with anti–PD-1 antibody treatment; scale bars, 100 μm (left), 20 μm (right). **G–I,** Quantification of KRT17 expression, CD3 and CD8 in all 30 human colorectal cancer samples, including 15 (each) responders and non-responders. **J,** ROC curve for the prognostic prediction model based on KRT17 expression. **K,** Schematic summarizing our proposed model for the CTL infiltration under KRT17 expression in colorectal cancer. KRT17 inhibits colorectal cancer immune evasion by ubiquitin-mediated degradation of YTHDF2 to decrease m^{6}A-modified CXCL10 mRNA decay, which promotes CTL trafficking into tumor. Values are represented as mean ± SD. ROC, receiver operating characteristic; *, $P < 0.05$; **, $P < 0.01$; ***, $P < 0.001$; ns (no significance), by two-tailed Student *t* test (**G–I**); two-way ANOVA (**B–E**).

cytotoxicity (48). Collectively, these studies have shown that tumor cells enable immune escape at the transcriptional level by many epigenetic mechanisms. N6-methyladenosine (m^6A) RNA methylation is the most common and conserved internal modification in RNA in eukaryotic cells (23, 49). Nevertheless, the RNA epitranscriptome's role in T-lymphocyte migration remains poorly understood. We uncovered a relationship between reversible m^6A methylation with T-lymphocyte migration through the dynamic process of m^6A-modified mRNA transcripts. We also revealed that KRT17 induced T-lymphocyte migration by preserving CXCL10 expression in an m^6A-dependent manner. These data support the concept that CXCL10 is more abundant in dMMR colorectal cancer compared with pMMR colorectal cancer (11).

Despite the well-known breakthrough of immunotherapy, patients with colorectal cancer with pMMR status do not respond effectively to any immunotherapy alone. This is particularly concerning because patients with colorectal cancer with pMMR account for the largest proportion of colorectal cancer (27). The lack of T-lymphocyte infiltration into the tumor seems to be the main cause for this ineffectiveness. Therefore, there is interest in developing rational combinations that attract T lymphocytes into tumors of this type. Some preclinical and clinical studies have shown that combination of immunotherapy with radiotherapy, high-dose IL2, and IL10 have apparent responses in both melanoma and renal cell carcinoma through $CD8^+$ T-cell expansion (50, 51). However, this response is dependent on continued high-dose drug therapy. The toxicity of such combinations has been a concern for physicians and has limited the development of combination tumor immunotherapy. Our results showed that KRT17 promoted ubiquitination-mediated degradation of YTHDF2, which decreased the decay of CXCL10 m^6A transcript and increased T-lymphocyte infiltration in the presence of IFNγ. This suggests that increased T-lymphocyte infiltration leads to more IFNγ secretion into the TME, which in turn leads to increased CXCL10 expression and continues to attract more T lymphocytes. This positive feedback of T-lymphocyte infiltration may be initialized by low-dose and intermittent medication in tumors with high expression KRT17, which would avoid high-dose drug toxicity. Given this, our approach has great potential clinical value.

With the astounding achievement of ICIs therapies in recent years, there remains an urgent need to find effective markers that can distinguish patients who will significantly benefit from ICI therapy. Reduced CTL infiltration represents the most recognized reason. Herein, we found that KRT17 overexpression in tumor cells could enhance immunotherapy response in an immunotherapy-resistant model by the YTHDF2–CXCL10 axis. Therefore, gene-modifying techniques, such as CRISPR–Cas9 combined with targeting guide RNA (52), antibody-delivered short interfering RNA (53), or aptamer–short interfering RNA chimeras (54), can be used to modify KRT17–YTHDF2–CXCL10 axis in tumor cells, although this possibility requires further study. Moreover, although dMMR and microsatellite instability-high are the recognized predictors of ICI response in colorectal cancer (9), but some mutations in pMMR tumors may be also recognized by the immune system. There remain other unknown immune system regulators. Thus, the number of $CD8^+$ cells is usually considered an indicator of response (55, 56). Specifically, KRT17 expression was a better predictor of ICI responsiveness than $CD3^+$ or $CD8^+$ density in endoscopic biopsy samples, which might be a promising clinical marker for immunotherapy in colorectal cancer. Our other major prospective clinical trial, which aims to investigate the effect of T-lymphocyte infiltration on the response to immunotherapy in rectal cancer, is ongoing (ClinicalTrials.gov, Number NCT 05450029). We will validate KRT17 as an immunotherapy biomarker based on this prospective clinical trial. A randomized controlled study targeting KRT17 might then be conducted to determine whether KRT17 could be used as an immunotherapy marker for clinical promotion in colorectal cancer.

Conclusions

We found that KRT17 was highly expressed in dMMR tumors, increased CTL infiltration into tumors, and sensitized responses to ICIs in colorectal cancer. This immune effect was mediated by elevated CXCL10 expression, whose mRNA transcript was stabilized owing to proteolytic degradation of the m^6A reader YTHDF2. Our research demonstrates the critical role of KRT17 in reversing tumor escape and immunotherapy resistance. KRT17 also offers an opportunity to tackle the clinical problem of reduced immunotherapy response in pMMR tumors.

Authors' Disclosures

No disclosures were reported.

Authors' Contributions

W. Liang: Validation, investigation, writing–original draft. **H. Liu:** Investigation, methodology. **Z. Zeng:** Investigation, visualization. **Z. Liang:** Formal analysis. **H. Xie:** Formal analysis. **W. Li:** Data curation. **L. Xiong:** Software. **Z. Liu:** Software. **M. Chen:** Data curation. **H. Jie:** Formal analysis. **X. Zheng:** Project administration, writing–review and editing. **L. Huang:** Resources, funding acquisition. **L. Kang:** Conceptualization, resources, funding acquisition, writing–review and editing.

Acknowledgments

This work is supported by National Natural Science Foundation of China (82200569 and 82000515), China Postdoctoral Science Foundation (2021M703723), Basic and Applied Basic Research Foundation of Guangdong Province (2022A1515012498, 2021A1515111011, and 2019A1515110043). This work is also supported by Science and Technology Projects in Guangzhou (202206010062), Science and Technology Key Research and Development Plan Project of Guangzhou (China; 202103000072), Sun Yat-sen University Clinical Research 5010 Program (2016005), Shenzhen "San Ming Projects" Research (grant no. lc202002) and National Key Clinical Discipline. The authors are grateful to all of the patients, research investigators, and study staff who took part in this study.

The publication costs of this article were defrayed in part by the payment of publication fees. Therefore, and solely to indicate this fact, this article is hereby marked "advertisement" in accordance with 18 USC section 1734.

Note

Supplementary data for this article are available at Cancer Immunology Research Online (http://cancerimmunolres.aacrjournals.org/).

Received October 13, 2022; revised January 26, 2023; accepted April 27, 2023; published first May 2, 2023.

Reference

1. Yang L, Li A, Lei Q, Zhang Y. Tumor-intrinsic signaling pathways: key roles in the regulation of the immunosuppressive tumor microenvironment. J Hematol Oncol 2019;12:125.
2. Hochman MJ, DeZern AE. Myelodysplastic syndrome and autoimmune disorders: two sides of the same coin? Lancet Haematol 2022;9:e523–e34.

3. Cohen EEW, Soulieres D, Le Tourneau C, Dinis J, Licitra L, Ahn MJ, et al. Pembrolizumab versus methotrexate, docetaxel, or cetuximab for recurrent or metastatic head-and-neck squamous cell carcinoma (KEYNOTE-040): a randomised, open-label, phase 3 study. Lancet 2019;393:156–67.
4. Schmid P, Cortes J, Pusztai L, McArthur H, Kummel S, Bergh J, et al. Pembrolizumab for early triple-negative breast cancer. N Engl J Med 2020; 382:810–21.
5. Dunn GP, Bruce AT, Ikeda H, Old LJ, Schreiber RD. Cancer immunoediting: from immunosurveillance to tumor escape. Nat Immunol 2002;3:991–8.
6. Bruni D, Angell HK, Galon J. The immune contexture and immunoscore in cancer prognosis and therapeutic efficacy. Nat Rev Cancer 2020;20:662–80.
7. Takeuchi Y, Tanegashima T, Sato E, Irie T, Sai A, Itahashi K, et al. Highly immunogenic cancer cells require activation of the WNT pathway for immunological escape. Sci Immunol 2021;6:eabc6424.
8. Harlin H, Meng Y, Peterson AC, Zha Y, Tretiakova M, Slingluff C, et al. Chemokine expression in melanoma metastases associated with $CD8^+$ T-cell recruitment. Cancer Res 2009;69:3077–85.
9. Le DT, Durham JN, Smith KN, Wang H, Bartlett BR, Aulakh LK, et al. Mismatch repair deficiency predicts response of solid tumors to PD-1 blockade. Science 2017;357:409–13.
10. Huang Y, Yuan J, Righi E, Kamoun WS, Ancukiewicz M, Nezivar J, et al. Vascular normalizing doses of antiangiogenic treatment reprogram the immunosuppressive tumor microenvironment and enhance immunotherapy. Proc Natl Acad Sci U S A 2012;109:17561–6.
11. Galon J, Costes A, Sanchez-Cabo F, Kirilovsky A, Mlecnik B, Lagorce-Pages C, et al. Type, density, and location of immune cells within human colorectal tumors predict clinical outcome. Science 2006;313:1960–4.
12. Pages F, Mlecnik B, Marliot F, Bindea G, Ou FS, Bifulco C, et al. International validation of the consensus immunoscore for the classification of colon cancer: a prognostic and accuracy study. Lancet 2018;391:2128–39.
13. Tumeh PC, Harview CL, Yearley JH, Shintaku IP, Taylor EJ, Robert L, et al. PD-1 blockade induces responses by inhibiting adaptive immune resistance. Nature 2014;515:568–71.
14. Langmead B, S SL. Fast gapped-read alignment with Bowtie 2. Nat Methods 2012;9:357–9.
15. Perez-Riverol Y, Csordas A, Bai J, Bernal-Llinares M, Hewapathirana S, Kundu DJ, et al. The PRIDE database and related tools and resources in 2019: improving support for quantification data. Nucleic Acids Res 2019;47:D442–D50.
16. Cao J, Wu X, Qin X, Li Z. Uncovering the effect of passage number on HT29 cell line based on the cell metabolomic approach. J Proteome Res 2021;20:1582–90.
17. Kawazu M, Ueno T, Saeki K, Sax N, Togashi Y, Kanaseki T, et al. HLA class I analysis provides insight into the genetic and epigenetic background of immune evasion in colorectal cancer with high microsatellite instability. Gastroenterology 2022;162:799–812.
18. Park BV, Freeman ZT, Ghasemzadeh A, Chattergoon MA, Rutebemberwa A, Steigner J, et al. TGFbeta1-mediated SMAD3 enhances PD-1 expression on antigen-specific T cells in cancer. Cancer Discov 2016;6:1366–81.
19. Fei Q, Zou Z, Roundtree IA, Sun HL, He C. YTHDF2 promotes mitotic entry and is regulated by cell-cycle mediators. PLoS Biol 2020;18:e3000664.
20. Hou G, Zhao X, Li L, Yang Q, Liu X, Huang C, et al. SUMOylation of YTHDF2 promotes mRNA degradation and cancer progression by increasing its binding affinity with m6A-modified mRNAs. Nucleic Acids Res 2021;49:2859–77.
21. Xu F, Li J, Ni M, Cheng J, Zhao H, Wang S, et al. FBW7 suppresses ovarian cancer development by targeting the N(6)-methyladenosine binding protein YTHDF2. Mol Cancer 2021;20:45.
22. Paris J, Morgan M, Campos J, Spencer GJ, Shmakova A, Ivanova I, et al. Targeting the RNA m(6)A reader YTHDF2 selectively compromises cancer stem cells in acute myeloid leukemia. Cell Stem Cell 2019;25:137–48.
23. Wang X, Lu Z, Gomez A, Hon GC, Yue Y, Han D, et al. N6-methyladenosine-dependent regulation of messenger RNA stability. Nature 2014;505:117–20.
24. van der Woude LL, Gorris MAJ, Halilovic A, Figdor CG, de Vries IJM. Migrating into the tumor: a roadmap for T cells. Trends Cancer 2017;3:797–808.
25. Wang L, Hui H, Agrawal K, Kang Y, Li N, Tang R, et al. m(6) A RNA methyltransferases METTL3/14 regulate immune responses to anti–PD-1 therapy. EMBO J 2020;39:e104514.
26. Yang S, Wei J, Cui YH, Park G, Shah P, Deng Y, et al. m(6)A mRNA demethylase FTO regulates melanoma tumorigenicity and response to anti–PD-1 blockade. Nat Commun 2019;10:2782.
27. Ganesh K, Stadler ZK, Cercek A, Mendelsohn RB, Shia J, Segal NH, et al. Immunotherapy in colorectal cancer: rationale, challenges, and potential. Nat Rev Gastroenterol Hepatol 2019;16:361–75.
28. Llosa NJ, Cruise M, Tam A, Wicks EC, Hechenbleikner EM, Taube JM, et al. The vigorous immune microenvironment of microsatellite instable colon cancer is balanced by multiple counter-inhibitory checkpoints. Cancer Discov 2015;5:43–51.
29. Smyrk TC, Watson P, Kaul K, Lynch HT. Tumor-infiltrating lymphocytes are a marker for microsatellite instability in colorectal carcinoma. Cancer 2001;91: 2417–22.
30. Phillips SM, Banerjea A, Feakins R, Li SR, Bustin SA, Dorudi S. Tumour-infiltrating lymphocytes in colorectal cancer with microsatellite instability are activated and cytotoxic. Br J Surg 2004;91:469–75.
31. Segal NH, Parsons DW, Peggs KS, Velculescu V, Kinzler KW, Vogelstein B, et al. Epitope landscape in breast and colorectal cancer. Cancer Res 2008;68:889–92.
32. Liang ZX, Liu HS, Xiong L, Yang X, Wang FW, Zeng ZW, et al. A novel NF-kappaB regulator encoded by circPLCE1 inhibits colorectal carcinoma progression by promoting RPS3 ubiquitin-dependent degradation. Mol Cancer 2021;20:103.
33. Zhou C, Liu HS, Wang FW, Hu T, Liang ZX, Lan N, et al. circCAMSAP1 promotes tumor growth in colorectal cancer via the miR-328–5p/E2F1 axis. Mol Ther 2020;28:914–28.
34. Escobar-Hoyos LF, Yang J, Zhu J, Cavallo JA, Zhai H, Burke S, et al. Keratin 17 in premalignant and malignant squamous lesions of the cervix: proteomic discovery and immunohistochemical validation as a diagnostic and prognostic biomarker. Mod Pathol 2014;27:621–30.
35. Regenbogen E, Mo M, Romeiser J, Shroyer ALW, Escobar-Hoyos LF, Burke S, et al. Elevated expression of keratin 17 in oropharyngeal squamous cell carcinoma is associated with decreased survival. Head Neck 2018;40:1788–98.
36. Chivu-Economescu M, Dragu DL, Necula LG, Matei L, Enciu AM, Bleotu C, et al. Knockdown of KRT17 by siRNA induces antitumoral effects on gastric cancer cells. Gastric Cancer 2017;20:948–59.
37. Quinn JJ, Jones MG, Okimoto RA, Nanjo S, Chan MM, Yosef N, et al. Single-cell lineages reveal the rates, routes, and drivers of metastasis in cancer xenografts. Science 2021;371:eabc1944.
38. Depianto D, Kerns ML, Dlugosz AA, Coulombe PA. Keratin 17 promotes epithelial proliferation and tumor growth by polarizing the immune response in skin. Nat Genet 2010;42:910–4.
39. Chung BM, Arutyunov A, Ilagan E, Yao N, Wills-Karp M, Coulombe PA. Regulation of C–X–C chemokine gene expression by keratin 17 and hnRNP K in skin tumor keratinocytes. J Cell Biol 2015;208:613–27.
40. Hobbs RP, DePianto DJ, Jacob JT, Han MC, Chung BM, Batazzi AS, et al. Keratin-dependent regulation of Aire and gene expression in skin tumor keratinocytes. Nat Genet 2015;47:933–8.
41. Wang W, Lozar T, Golfinos AE, Lee D, Gronski E, Ward-Shaw E, et al. Stress keratin 17 expression in head and neck cancer contributes to immune evasion and resistance to immune-checkpoint blockade. Clin Cancer Res 2022;28: 2953–68.
42. Yu R, Li Q, Feng Z, Cai L, Xu Q. m6A Reader YTHDF2 regulates LPS-induced inflammatory response. Int J Mol Sci 2019;20:1323.
43. Wu C, Chen W, He J, Jin S, Liu Y, Yi Y, et al. Interplay of m6A and H3K27 trimethylation restrains inflammation during bacterial infection. Sci Adv 2020; 6:eaba0647.
44. Chung BM, Murray CI, Van Eyk JE, Coulombe PA. Identification of novel interaction between annexin A2 and keratin 17: evidence for reciprocal regulation. J Biol Chem 2012;287:7573–81.
45. Su R, Dong L, Li C, Nachtergaele S, Wunderlich M, Qing Y, et al. R-2HG exhibits antitumor activity by targeting FTO/m(6)A/MYC/CEBPA signaling. Cell 2018; 172:90–105.
46. Peng D, Kryczek I, Nagarsheth N, Zhao L, Wei S, Wang W, et al. Epigenetic silencing of TH1-type chemokines shapes tumour immunity and immunotherapy. Nature 2015;527:249–53.
47. Zingg D, Arenas-Ramirez N, Sahin D, Rosalia RA, Antunes AT, Haeusel J, et al. The histone methyltransferase Ezh2 controls mechanisms of adaptive resistance to tumor immunotherapy. Cell Rep 2017;20:854–67.
48. Pan D, Kobayashi A, Jiang P, Ferrari de Andrade L, Tay RE, Luoma AM, et al. A major chromatin regulator determines resistance of tumor cells to T-cell–mediated killing. Science 2018;359:770–5.
49. Zhao BS, Roundtree IA, He C. Post-transcriptional gene regulation by mRNA modifications. Nat Rev Mol Cell Biol 2017;18:31–42.
50. Bentebibel SE, Hurwitz ME, Bernatchez C, Haymaker C, Hudgens CW, Kluger HM, et al. A first-in-human study and biomarker analysis of NKTR-214, a novel IL2Rbetagamma-biased cytokine, in patients with advanced or metastatic solid tumors. Cancer Discov 2019;9:711–21.

51. Naing A, Infante JR, Papadopoulos KP, Chan IH, Shen C, Ratti NP, et al. PEGylated IL-10 (Pegilodecakin) induces systemic immune activation, CD8(+) T-cell invigoration and polyclonal T-cell expansion in cancer patients. Cancer Cell 2018;34:775–91.
52. Ma Y, Yu L, Pan S, Gao S, Chen W, Zhang X, et al. CRISPR/Cas9-mediated targeting of the Rosa26 locus produces Cre reporter rat strains for monitoring Cre–loxP-mediated lineage tracing. FEBS J 2017;284:3262–77.
53. Yao YD, Sun TM, Huang SY, Dou S, Lin L, Chen JN, et al. Targeted delivery of PLK1-siRNA by ScFv suppresses $Her2^{+}$ breast cancer growth and metastasis. Sci Transl Med 2012;4:130ra48.
54. Su S, Liao J, Liu J, Huang D, He C, Chen F, et al. Blocking the recruitment of naive CD4(+) T cells reverses immunosuppression in breast cancer. Cell Res 2017;27:461–82.
55. Feng Z, Puri S, Moudgil T, Wood W, Hoyt CC, Wang C, et al. Multispectral imaging of formalin-fixed tissue predicts ability to generate tumor-infiltrating lymphocytes from melanoma. J Immunother Cancer 2015;3:47.
56. Liu H, Liang Z, Cheng S, Huang L, Li W, Zhou C, et al. Mutant KRAS drives immune evasion by sensitizing cytotoxic T cells to activation-induced cell death in colorectal cancer. Adv Sci (Weinh) 2023;10:e2203757.